



# Finite element formulation for modeling nonlinear viscoelastic elastomers

Pedro Areias<sup>a,1</sup>, Karel Matouš<sup>a,b,\*</sup>

<sup>a</sup> Computational Science and Engineering, University of Illinois at Urbana-Champaign, Urbana, IL 61801, USA

<sup>b</sup> Department of Aerospace Engineering, University of Illinois at Urbana-Champaign, Urbana, IL 61801, USA

## ARTICLE INFO

### Article history:

Received 10 November 2007

Received in revised form 22 February 2008

Accepted 17 June 2008

Available online 5 July 2008

### Keywords:

Stabilized element

Implicit gradient

Integration algorithm

Viscoelasticity

Propellant unit cell

## ABSTRACT

Nonlinear viscoelastic response of reinforced elastomers is modeled using a three-dimensional mixed finite element method with a nonlocal pressure field. A general second-order unconditionally stable exponential integrator based on a diagonal Padé approximation is developed and the Bergström–Boyce nonlinear viscoelastic law is employed as a prototype model. An implicit finite element scheme with consistent linearization is used and the novel integrator is successfully implemented. Finally, several viscoelastic examples, including a study of the unit cell for a solid propellant, are solved to demonstrate the computational algorithm and relevant underlying physics.

© 2008 Elsevier B.V. All rights reserved.

## 1. Introduction

Particle-reinforced elastomers are used in variety of applications, such as solid propellants and automobile tires. The constitutive description of this important category of materials is a challenging research topic. The interacting physical processes taking place at various length and time scales make the modeling difficult: there is a large mismatch in stiffness between the matrix and the reinforcing particles, and large deformations of the quasi-incompressible nonlinear viscoelastic matrix, particle debonding, void growth, matrix tearing, Mullins hysteretic effect under cyclic loading, and other complex phenomena are also present.

Homogenized continuum models are usually used to capture some of these phenomena. Drozdov and Dorfmann [12], for example, used the network theory of rubber elasticity to capture the nonlinear equilibrium response of filled and unfilled elastomers. A similar approach was taken by Bergström and Boyce [6,7], who proposed a dual network model to predict the nonlinear viscoelastic response of carbon-black reinforced rubbers, with emphasis on capturing the large deformations and Mullins effects. Miehe and Göktepe [27] introduced a micromechanics-based micro-sphere model to represent viscoelasticity of elastomers. Purely phenomenological continuum laws of varying complexity are also often em-

ployed. Examples include Dorfmann and Ogden's analysis of the Mullins effect [11] and Simo's work on the finite-strain viscoelastic damage model [35]. One of the most comprehensive studies focusing on viscoelasticity and its numerical aspects is that of Reese and Govindjee [34].

Another issue is associated with the numerical analysis of these materials. The matrix material is highly nonlinear and nearly incompressible, so a special numerical framework must be employed. In principle, stable methods for the Stokes equation (see, e.g., Zienkiewicz and Wu [39]) can be adapted, with minor modifications, to finite strain problems. For incompressible bulk deformation, relatively high performance mixed elements were proposed, among others, by Hughes et al. [17], Chiumenti et al. [10] and Ramesh and Maniatty [33]. Recently, Puso and Solberg [32] proposed an element involving a convex combination with nodal quadrature, Tian et al. [38] developed a general purpose tetrahedral element with a good balance of properties, and Hauret et al. [15] introduced a diamond element based on discrete mechanics. In this work, we use the nonlocal pressure element developed by Areias and Matouš [1].

A related challenge is integrating the constitutive equations (ODEs), which are usually stiff and highly nonlinear. An implicit exponential integrator, for example, which is well suited for stiff and highly oscillatory problems has been used in elasto- and viscoplasticity [5]. For classical viscoelasticity, Fancello et al. [13] used this integrator in the context of the variational update.

In a series of recent papers, we have focused on decohesion of particles from a matrix [24–26]. In this work, the highly nonlinear viscoelastic response of a binder is investigated, with emphasis on the efficient integration algorithm. The highly nonlinear dependence

\* Corresponding author. Address: Computational Science and Engineering, University of Illinois at Urbana-Champaign, Urbana, IL 61801, USA. Tel.: +1 217 333 8448.

E-mail address: [matous@uiuc.edu](mailto:matous@uiuc.edu) (K. Matouš).

URL: <http://www.csar.uiuc.edu/~matous/> (K. Matouš).

<sup>1</sup> US Department of Energy, B341494. Alliant Techsystems, ATK-21316.

of the stress in the flow law and the plasticity-like idealization cannot, in general, make use of the Prony series method. Thus, we use the viscoelastic model proposed by Bergström and Boyce [6,7] and develop a new exponential integrator based on a diagonal Padé rational approximation, which has a number of advantages such as A-stability [19] and simplified calculation of derivatives. The exact preservation of a unit determinant by the Padé approximation in 2D and the supremum and infimum of determinant in 3D are also demonstrated. This result, which to the authors' knowledge is new, may have some practical importance.

We propose here a special numerical scheme, which was found to be required for two reasons:

1. The Bergström–Boyce constitutive equations could not be integrated effectively in the general case with traditional exponential integrator.
2. The proposed scheme can be applied to finite strain inelastic anisotropic materials.

Direct application to anisotropic materials results from a specific, anisotropic, flow law and its integration. This is not possible with classical integration schemes for *nonlinear* viscous laws; examples for *linear* viscous laws are well known in the literature [16].

The paper is organized as follows: in Section 2, we briefly describe the governing equations and highlight our mixed formulation with nonlocal pressure [1]. Section 3 details the constitutive model including the new Padé integrator and consistent linearization, and a particularization is constructed for the Bergström–Boyce model. Section 4 is devoted to numerical examples with emphasis on the numerical integration. Several viscoelastic examples are solved to demonstrate the computational algorithm and complexity of the underlying physics.

### 2. Mixed finite element method

Let  $\Omega_0 \subset \mathbb{R}^3$  represent the reference configuration of a given body. Given a certain point  $X, X \in \Omega_0$  identifies a material position as shown in Fig. 1. If the body contains no discontinuities, there is a unique mapping  $\varphi(X)$  such that  $\mathbf{x} \equiv \varphi(X)$  with  $\mathbf{x} = \mathbf{X} + \mathbf{u}$ , where  $\mathbf{u}$  is the displacement vector. Next, we introduce  $\mathbf{F} = \nabla_0 \varphi(X)$  as the deformation gradient, with Jacobian given by  $J = \det(\mathbf{F})$ , and we define left  $\mathbf{B} = \mathbf{F}\mathbf{F}^T$  and right  $\mathbf{C} = \mathbf{F}^T\mathbf{F}$  Cauchy–Green deformation tensors, respectively. Here,  $\nabla_0$  is the gradient with respect to  $\mathbf{X}$ .

The equilibrium equations and boundary conditions involve the stress, body forces, surface loads, and prescribed displacements

$$\begin{aligned} \nabla_0 \cdot \mathbf{P}^T + \mathbf{B}_0 &= \mathbf{0} \text{ in } \Omega_0, \\ \mathbf{u} &= \bar{\mathbf{u}} \text{ on } \Gamma_{\bar{\mathbf{u}}}, \\ \mathbf{P} \cdot \mathbf{N}_0 &= \bar{\mathbf{t}}_0 \text{ on } \Gamma_{\bar{\mathbf{t}}_0}, \end{aligned} \tag{1}$$

where  $\mathbf{P}$  is the first Piola–Kirchhoff stress tensor,  $\bar{\mathbf{u}}$  is the known displacement on the boundary  $\Gamma_{\bar{\mathbf{u}}}$ ,  $\bar{\mathbf{t}}_0$  is the known surface load on the boundary  $\Gamma_{\bar{\mathbf{t}}_0}$ , and  $\mathbf{N}_0 = 1/\sqrt{\mathbf{n} \cdot (\mathbf{B}\mathbf{n})}\mathbf{F}^T\mathbf{n}$ , where  $\mathbf{n}$  represents the unit normal to  $\Gamma_{\bar{\mathbf{t}}}$ . The boundary of the body is  $\Gamma = \Gamma_{\bar{\mathbf{u}}} \cup \Gamma_{\bar{\mathbf{t}}}$  with  $\Gamma_{\bar{\mathbf{u}}} \cap \Gamma_{\bar{\mathbf{t}}} = \emptyset$ .

After introducing the strain energy density function,  $\hat{w}(\mathbf{u}) \equiv \hat{w}(\mathbf{F})$ , which measures the stored energy in each point of the body as a function of its motion, and including  $\bar{\mathbf{t}}$  in the volume term (by means of generalized functions), the work function (Lagrangian functional) is calculated by integrating the strain energy density function  $\hat{w}$  and a constant body force  $\mathbf{B}_0$

$$\mathcal{L}(\mathbf{u}) = \int_{\Omega_0} [\rho_0 \hat{w}(\mathbf{F}) + \mathbf{B}_0 \cdot \mathbf{u}] dV, \tag{2}$$

where  $\rho_0 = J\rho$  is the reference mass density and  $\rho$  denotes the deformed mass density. From stationarity of the work function, equilibrium equations are obtained.

For completeness, we now summarize the mixed formulation with nonlocal pressure proposed by Areias and Matouš [1]. We use a continuous mixed pressure–displacement weak formulation and a bubble enhanced displacement field. To model the pressure spreading effect we adopt a strongly nonlocal implicit gradient model using the implicit version of Peerlings et al. [30]. The result is a finite strain extension of the MINI element [3] with a gradient term ( $P1 + \text{bubble}/P1 + \nabla\pi$ ). We denote this element as  $4/3cg$ . Simplified version of the element (obtained by removing the bubble) can be also obtained from this formulation [1].

The volume preserving part of the deformation gradient is calculated from the following decomposition:

$$\hat{\mathbf{F}} = J^{-\frac{1}{3}}\mathbf{F}. \tag{3}$$

Next, we introduce  $\bar{\mathbf{F}} = \theta^{\frac{1}{3}}\hat{\mathbf{F}}$  as a mixed deformation gradient, and  $\theta$  as an additional variable denoting a mixed representation for the Jacobian,  $\theta \equiv \det(\bar{\mathbf{F}})$ . In the finite element formulation,  $J = \theta$ , is satisfied in a weak sense.

The Kirchhoff stress is obtained using the relation by Coleman:

$$\boldsymbol{\tau} = \rho_0 \frac{\partial \hat{w}(\mathbf{F})}{\partial \mathbf{F}} \mathbf{F}^T \iff \boldsymbol{\tau} = \mathbf{P}\mathbf{F}^T, \tag{4}$$

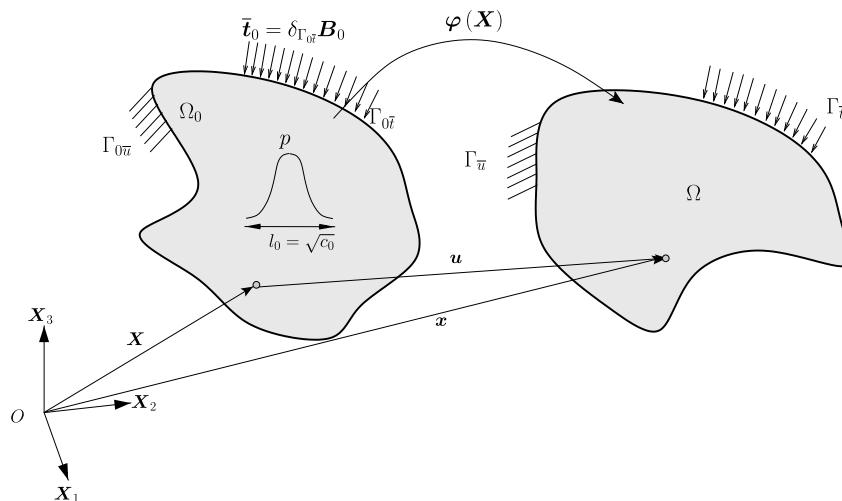


Fig. 1. Problem description: pressure spreading is controlled by parameter  $c_0$ .

and its deviatoric part reads

$$\mathbf{T} = \boldsymbol{\tau} - \tilde{\pi} \mathbf{1}, \quad (5)$$

where  $\tilde{\pi} = 1/3\text{tr}(\boldsymbol{\tau})$  represents the Kirchhoff hydrostatic pressure and  $\mathbf{1}$  is the second-order identity tensor. Satisfaction of poly-convexity requires a convex volumetric energy,  $U(J)$ , such that  $\tilde{\pi} = JdU(J)/dJ$ .

The following equations are provided for  $\tilde{\pi}$  and  $\pi$ :

$$\begin{aligned} \tilde{\pi} &\equiv g(J) = \kappa[J^2 - J + \ln(J)], \\ \pi &\equiv g(\theta) = \kappa[\theta^2 - \theta + \ln(\theta)], \end{aligned} \quad (6)$$

and

$$\theta = g^{-1}(\pi). \quad (7)$$

The bulk modulus is  $\kappa$ ,  $\pi$  and  $\theta$  are pressure-like and dilatation-like quantities, respectively. The function  $g^{-1}$  is obtained only implicitly, since there is no closed-form inverse of  $g$ . Due to direct application of the Galerkin method, the relationship between volumetric energy  $U(J)$ , which would enter the functional  $\overline{\mathcal{F}}$  mentioned below, and  $g(J)$  is not needed.

To force pressure spreading, the pressure field  $\pi$  obeys the following inhomogeneous form of the Helmholtz equation:

$$\pi - c_0 \Delta_0 \pi - \tilde{\pi} = 0, \quad (8)$$

where  $\Delta_0$  is the Laplace operator with respect to the material coordinates. Here, the area parameter  $c_0$  controls the degree of nonlocality of the pressure field. Please note that Eq. (8) will introduce an approximation of the same order of magnitude as the one induced by the explicit gradient model

$$\pi = \tilde{\pi} + c_0 \nabla \tilde{\pi}, \quad (9)$$

which would require  $\mathcal{C}^1$ -continuity of the pressure field, whereas implicit approach enables a straightforward  $\mathcal{C}^0$  finite element interpolation. A weak form of (8) is obtained by using the test function  $\zeta$

$$\int_{\Omega_0} \zeta (\pi - \tilde{\pi}) dV_0 + c_0 \int_{\Omega_0} \nabla_0 \zeta \cdot \nabla_0 \pi dV_0 = 0 \quad (10)$$

$\forall \zeta \in [\mathcal{H}^1(\Omega_0)]^1$ , where  $[\mathcal{H}^1(\Omega_0)]^{n_{sd}}$  denotes the Sobolev space of square-integrable functions with weak derivatives up to first order with range in  $\mathbb{R}^{n_{sd}}$ . We make use of the Lasry–Belytschko boundary conditions for the pressure [20].

After applying standard variational methods and using (10), we state the equilibrium condition and its first variation using a mixed form: Find  $\mathbf{u}(X)$  and  $\pi(X)$  such that

$$\begin{aligned} \delta \overline{\mathcal{F}}(\mathbf{u}; \pi) &= \int_{\Omega_0} \left\{ \underbrace{[\boldsymbol{\tau} + (\pi - \tilde{\pi}) \mathbf{1}] : \nabla \mathbf{v}}_{\tilde{\boldsymbol{\tau}}} \right. \\ &\quad \left. + \zeta [\pi - g(J)] + c_0 \nabla_0 \zeta \cdot \nabla_0 \pi + \mathbf{B}_0 \cdot \mathbf{v} \right\} dV_0 = 0 \\ \Delta \delta \overline{\mathcal{F}}(\mathbf{u}; \pi) &= \int_{\Omega_0} \left\{ \nabla \mathbf{v} : \mathcal{C}_{TL} : \nabla \Delta \mathbf{u} - \frac{1}{3} \nabla \mathbf{v} : [\mathbf{1} \otimes (\mathbf{1} : \mathcal{C}_{TL} : \nabla \Delta \mathbf{u})] \right. \\ &\quad \left. - \tilde{\boldsymbol{\tau}} : (\nabla \mathbf{v} \nabla \Delta \mathbf{u}) + \Delta \pi \mathbf{1} : \nabla \mathbf{v} + \zeta \Delta \pi \right. \\ &\quad \left. - J \zeta \frac{dg}{dJ} \mathbf{1} : \nabla \Delta \mathbf{u} + c_0 \nabla_0 \zeta \cdot \nabla_0 \Delta \pi \right\} dV_0, \end{aligned} \quad (11)$$

for all  $\mathbf{v}$  and  $\zeta$  satisfying

$$\mathbf{v} \in [\mathcal{H}^1(\Omega_0)]^3 \wedge \zeta \in [\mathcal{H}^1(\Omega_0)]^1, \quad \mathbf{v} = \mathbf{0} \text{ on } \Gamma_{0\bar{u}}. \quad (12)$$

Here,  $\nabla \cdot = \nabla_0 \cdot \mathbf{F}^{-1}$  is a gradient with respect to the spatial configuration. Note that both the Kirchhoff stress tensor  $\boldsymbol{\tau} = \mathbf{P}\mathbf{F}^T$  and the gradient of the test function  $\nabla \mathbf{v} = \delta \mathbf{F}\mathbf{F}^{-1}$  are independent of  $\theta$ , and that we can determine an instantaneous bulk modulus  $\kappa' = 1/\theta(g' - \pi/\theta)$ . Note that, the functional  $\overline{\mathcal{F}}(\mathbf{u}; \pi)$  is not explicitly

defined, since we directly use the Galerkin method leading to unsymmetric stiffness. The equilibrium stress  $\tilde{\boldsymbol{\tau}}$  is obtained as

$$\tilde{\boldsymbol{\tau}} = \mathbf{T} + \pi \mathbf{1} = \boldsymbol{\tau} + (\pi - \tilde{\pi}) \mathbf{1}. \quad (13)$$

The term  $\mathcal{C}_{TL}$  is the tangent modulus, related to the velocity gradient. If the constitutive stress is trace-free, then the time-derivative of  $\mathbf{T}$  is given by  $\dot{\mathbf{T}} = \mathcal{C}_{TL} : \mathbf{L}$ , with  $\mathbf{L} = \dot{\mathbf{F}}\mathbf{F}^{-1}$ . In our implementation, the initial stress term (third term in (11)) is preceded by a minus sign, which is distinct from the usual Lie derivative (or Oldroyd) modulus. Both the tangent and Oldroyd moduli are introduced in Section 3.2. It is worth noting that exact calculation of (11) is necessary to obtain quadratic convergence rate of Newton's method as demonstrated in Section 4.

### 3. Constitutive laws

Although the constitutive update scheme developed in this work is applicable to a wide range of nonlinear material models, we focus on the nonlinear viscoelastic response suitable for analysis of reinforced elastomers, such as solid propellants. We employ a viscoelastic constitutive law, without thermal effects, that is fully nonlinear (both the flow law and the elastic law are nonlinear) in the sense of Lion [22]. But we will maintain generality of the algorithm, which, with minor modifications, can be particularized to other problems such as finite strain plasticity with an arbitrary hyperelastic behavior (not only the traditional Hencky or St. Venant elastoplasticity). Here, we describe the general algorithm, and its particularization for the Bergström–Boyce model is presented in Section 3.3.

First, we introduce the multiplicative decomposition of the deformation gradient (see [21])

$$\mathbf{F} = \mathbf{F}_e \mathbf{F}_v, \quad (14)$$

where  $\mathbf{F}_e$  is the reversible (elastic) deformation gradient and  $\mathbf{F}_v$  denotes the viscous deformation gradient. The viscous deformation gradient satisfies

$$\det(\mathbf{F}_v) = 1. \quad (15)$$

The kinematic quantities, such as the viscous right Cauchy–Green tensor and the elastic left Cauchy–Green tensor, are given by

$$\begin{aligned} \mathbf{C}_v &= \mathbf{F}_v^T \mathbf{F}_v, \\ \mathbf{B}_e &= \mathbf{F}_e \mathbf{F}_e^T = \mathbf{F} \mathbf{C}_v^{-1} \mathbf{F}^T, \end{aligned} \quad (16)$$

and the relation between the deviatoric stress and the hyperelastic strain tensors reads

$$\mathbf{T} = \mathbf{T}(\mathbf{B}_e), \quad (17)$$

where elastic isotropy is assumed (cf. eq. 31, page 142 of [9]). It is easy to show that there exists a  $\tilde{w}(\mathbf{B}_e)$  such that  $\tilde{w}(\mathbf{F}) = \tilde{w}(\mathbf{B}_e)$  and the Kirchhoff stress is given by

$$\boldsymbol{\tau} = \rho_0 \frac{\partial \tilde{w}(\mathbf{F})}{\partial \mathbf{F}} \mathbf{F}^T = 2\rho_0 \frac{\partial \tilde{w}(\mathbf{B}_e)}{\partial \mathbf{B}_e} \mathbf{B}_e. \quad (18)$$

For an anisotropy one could use the second Piola–Kirchhoff stress, which is dependent on both  $\mathbf{C}$  and  $\mathbf{C}_v$  (see [2]).

The flow law follows the usual definition

$$\dot{\mathbf{F}}_v \mathbf{F}_v^{-1} \equiv \mathbf{D}_v = \dot{\gamma} \mathbf{N}, \quad (19)$$

and the flow vector is given by

$$\mathbf{N} = \mathbf{T} / \|\mathbf{T}\|_{\mathcal{F}}. \quad (20)$$

Note that  $\mathbf{N}$  is a symmetric tensor, and hence the viscous strain rate  $\mathbf{D}_v$  is the complete viscous velocity gradient. The form of the flow law also allows pre-existing anisotropy. The notation  $\|\cdot\|_{\mathcal{F}}$  is used here for the Frobenius norm of a given linear operator  $\cdot$ . Next, the

equivalent strain rate, expressed as a nonlinear function of the stress and the viscous right Cauchy–Green tensor, yields

$$\dot{\gamma} = \dot{\gamma}(\mathbf{C}_v, \mathbf{T}), \quad (21)$$

where the relation

$$\dot{\gamma} = \|\mathbf{D}_v\|_{\mathcal{F}} \quad (22)$$

holds by construction. The dependence of  $\dot{\gamma}$  upon  $\mathbf{C}_v$  and  $\mathbf{T}$  is effected by means of the two scalar functions  $f_v$  and  $T$  such that

$$\dot{\gamma} = \dot{\gamma}[f_v(\mathbf{C}_v), T(\mathbf{T})], \quad (23)$$

and, although not strictly required, the inverse relation

$$T = T[\dot{\gamma}, f_v(\mathbf{C}_v)] \equiv \|\mathbf{T}\|_{\mathcal{F}} \quad (24)$$

is assumed to be explicit. To inspect the interdependencies in (24), we rewrite it as

$$\dot{\mathbf{C}}_v = \underbrace{2\mathbf{F}_v^T \dot{\gamma}[f_v(\mathbf{C}_v), T(\mathbf{F}\mathbf{C}_v^{-1}\mathbf{F}^T)]}_{\mathbf{D}_v} \frac{\mathbf{T}(\mathbf{F}\mathbf{C}_v^{-1}\mathbf{F}^T)}{\|\mathbf{T}(\mathbf{F}\mathbf{C}_v^{-1}\mathbf{F}^T)\|_{\mathcal{F}}} \mathbf{F}_v, \quad (25)$$

along with the initial condition  $\mathbf{C}_v|_{t=0} = \mathbf{1}$  in the absence of pre-existing flow. Note that  $\mathbf{C}_v$  is the only unknown in this system, since  $\mathbf{F}$  is imposed. Also,  $\mathbf{F}_v$  is a function of  $\dot{\gamma}$ , and therefore, it is also a function of  $\mathbf{C}_v$ . This is a consequence of the evolution law's dependence on a symmetric vector, leaving a zero spin tensor  $\mathbf{W}_{v0}$ . Note about anisotropy is made when the integration algorithm is introduced. The determination of  $\mathbf{C}_v$  is described below.

### 3.1. Integration algorithm

For a prescribed deformation path, the stress response and the viscous multiplier evolution can be obtained by integrating the constitutive Eqs. (17) and (25). Since no closed form is available, the ODE system, which consists of the flow law after replacement of the elasticity relation must be solved numerically. The problem is a first-order ODE whose nonlinearity suggests the use of an implicit integrator. Although the eigenvalues of the flow matrix are bounded, the scaling parameter  $\dot{\gamma}$  often induces a stiff system. Thus, the choice of integrator is usually dictated by the particular requirements of the constitutive update. From the numerical methods available in the literature, we focus on a class of exponential integrators that are unconditionally stable, and thus are appealing for application in the finite element method.

Two related steps are required: integration and linearization. These operations are depicted in Fig. 3. The numerically integrated flow law is given by one of the following two forms:

$$\begin{aligned} (\mathbf{F}_v)_{n+1} &= \widetilde{\text{exp}}(\dot{\gamma}_{n+1}\Delta t\mathbf{N}_{n+1})(\mathbf{F}_v)_n, \\ (\mathbf{C}_v)_{n+1} &= (\mathbf{F}_v^T)_n \widetilde{\text{exp}}(2\dot{\gamma}_{n+1}\Delta t\mathbf{N}_{n+1})(\mathbf{F}_v)_n \end{aligned} \quad (26)$$

for general and symmetric flow vectors, respectively, where  $\widetilde{\text{exp}}$  is an approximation of the matrix exponential function. Note that for isotropic case,  $\mathbf{W}_v$  remains zero. However, for anisotropy  $\mathbf{F}_v$  is determined from the nonsymmetrized version of the flow law Eq. (19) and (26)<sub>1</sub>. There are no requirements of co-axiality of elastic measures and visco-elastic measures.

We assume that the deformation is known from the finite element method described in Section 2; in particular, all the primary quantities  $\mathbf{F}_n$ ,  $\tau_n$ ,  $\pi_n$ ,  $\gamma_n$  and  $T_n$  are known at time  $t_n$ , and the finite element approximations for the deformation gradient  $\mathbf{F}_{n+1}$  and the pressure  $\pi_{n+1}$  are given, where  $t_{n+1} \equiv t_n + \Delta t$  and  $\Delta t \in \mathbb{R}^+$  is an imposed time step.

There are at least 19 methods for approximating the exponential function of a matrix [28]. Among these, a diagonal Padé rational approximation has a number of advantages, including A-stability [19] and simplified calculation of derivatives. Therefore,

we present a novel exponential integrator based on Padé approximation and discuss its accuracy and conservation properties.

The  $q$ -diagonal Padé approximation of the exponential function of a matrix  $\mathbf{Z}$  yields

$$\widetilde{\text{exp}}_q(\mathbf{Z}) = \mathbf{D}_q(\mathbf{Z})^{-1}\mathbf{D}_q(-\mathbf{Z}), \quad (27)$$

where the matrix function  $\mathbf{D}_q(\mathbf{Z})$  is given by

$$\mathbf{D}_q(\mathbf{Z}) = \sum_{j=0}^q \frac{(2q-j)!q!}{(2q)j!(q-j)!} (-\mathbf{Z})^j. \quad (28)$$

With  $q = 1$ , for example, the well known Hughes–Winget formula

$$\widetilde{\text{exp}}_1(\mathbf{Z}) = \left(\mathbf{1} - \frac{1}{2}\mathbf{Z}\right)^{-1} \frac{\mathbf{Z}}{2} + \left(\mathbf{1} - \frac{1}{2}\mathbf{Z}\right)^{-1} \quad (29)$$

is obtained [18]. This formula is often used to extract an approximation to the rotation matrix from the spin tensor. In the numerical examples presented hereafter, we use  $q = 2$ .

An error analysis of the Padé approximation and error bounds are detailed in Appendix A.1. We also show in Appendix A.2 that for a traceless second-order tensor, a unit determinant is preserved in 2D and the supremum and infimum are shown in 3D, which is important for nearly-incompressible laws, where cumulative integration drift can cause substantial error in the incompressibility constraint. This result, to the authors' knowledge new, may have some practical importance. Finally, in Appendix A.3 we show that the integrator (26) using the two-term Padé approximation is second-order accurate, which makes the exponential integrator very competitive against the midpoint rule even in the context of infinitesimal strain (this property was intelligently explored by Artioli et al. [5]). The integrator is also unconditionally stable.

### 3.2. Constitutive update and linearization

We now provide a comprehensive description of the nonlinear constitutive solution and the exact calculation of the tangent modulus. As traditionally performed [37], we use a double nested iteration: (i) at the pointwise level (in order to solve the constitutive law); (ii) at the global level in order to solve the equilibrium equation. Locally, we employ the Newton–Raphson iterative method to obtain the viscous tensor  $\mathbf{C}_v$  and therefore the stress tensor. Contractivity, in the sense of Simo and Govindjee [36], is verified only for cases where two evolving states are sufficiently close that both the elastic moduli and the flow vector directions are similar to each other. As a consequence of several nonlinearities, a definitive answer is difficult to obtain and is omitted here.

We begin by stating the extended system with unknowns  $\mathbf{C}_v$  and  $\Delta\gamma$ . Note that  $\Delta\gamma$  is a redundant unknown, as it can be calculated from  $\mathbf{C}_v$ . However, the problem stated in  $\mathbf{C}_v$  is ill-posed, since for small  $\mathbf{F}$  one would obtain  $\text{exp}(2\dot{\gamma}\Delta t\mathbf{N}) = \mathbf{1}$ , which results in  $\dot{\gamma} = 0$ . Such a value produces a singularity in the Bergström–Boyce model described later. To circumvent this problem, Bergström and Boyce [7] introduced a numerical parameter  $\epsilon$ , but this did not eliminate ill-conditioning. When attempted, the direct approach halted frequently due to an inadmissible  $\mathbf{C}_v$  in the inner iteration. In contrast, the proposed extended system is always well posed, since  $\Delta\gamma$  is an additional unknown and can be close to zero resulting in  $(\mathbf{C}_v)_{n+1} \cong (\mathbf{C}_v)_n$ . Large time steps can be used, as will be shown.

In what follows, symmetric second-order tensors in Voigt notation are identified by an underline,  $\underline{\cdot}$ , whereas fourth-order tensors in Voigt notation use blackboard style. For example, the second-order tensor  $\mathbf{A}$  in Voigt notation reads  $\underline{\mathbf{A}}$ , and the fourth-order tensor  $\mathcal{A}$  (usually represented in calligraphic font) is  $\mathbb{A}$  in Voigt notation. Marked computational savings result from using this notation, since we can take advantage of symmetry in the multiplications.

Typically, the moduli calculated in Voigt notation must have the last three columns scaled so that the correct values are recovered. Note that in the literature some divergence in Voigt notation occurs, resulting in misleading versions of the flow vector. For example, if the gradient of a yield function is calculated *after* the replacement  $T_{ij} = T_{ji}$  is performed, then the flow vector is compatible with engineering notation for shear strains. Caution must be taken in calculating the derivatives and the consistent modulus; contractions of fourth-order tensors cannot be directly replaced by simple matrix products in Voigt notation. Moreover, to facilitate the derivations and take advantage of minor symmetry, two operators  $\mathbb{A}$  and  $\mathbb{B}$ , valid for general symmetric second-order tensors, are introduced. If  $\mathbf{A}$  is a given second-order tensor (not necessarily symmetric), then

$$\mathbb{A}(\mathbf{A})_{\cdot} = [\mathbf{A}^T \cdot \mathbf{A}] \Rightarrow \mathbb{A}(\mathbf{A}) = \frac{d[\mathbf{A}^T \cdot \mathbf{A}]}{d\cdot} \quad (30)$$

and

$$\mathbb{B}(\mathbf{A})_{\cdot} = \mathbb{A}(\mathbf{A}^T)_{\cdot} = \mathbf{A} \cdot \mathbf{A}^T, \quad (31)$$

where  $\cdot$  is a symmetric second-order tensor. With these operators, we use the compact notation

$$\underline{\mathbf{B}}_e = \mathbb{B}(\mathbf{F})\underline{\mathbf{C}}_v^{-1} \quad (32)$$

and

$$\frac{d\underline{\mathbf{C}}_v^{-1}}{dt} = -\mathbb{A}(\underline{\mathbf{C}}_v^{-1}) \frac{d\underline{\mathbf{C}}_v}{dt}. \quad (33)$$

Employing this nomenclature, the system (26)<sub>2</sub> and (24) can be written in the form

$$\text{eq}_1 \equiv (\underline{\mathbf{C}}_v)_{n+1} - \mathbb{A}(\mathbf{F}_v)_n \widehat{\text{exp}}(\mathbf{Z}_{n+1}) = 0, \quad (34)$$

$$\text{eq}_2 \equiv \mathbf{T}_{n+1} : \mathbf{T}_{n+1} - T_{n+1}^2(\Delta\gamma, \underline{\mathbf{C}}_v) = 0,$$

with

$$\mathbf{Z}_{n+1} = 2 \underbrace{\dot{\gamma}_{n+1} \Delta t}_{\Delta\gamma} \mathbf{N}_{n+1}. \quad (35)$$

Note that complementarity problems, such as rate-dependent elastoplasticity, can be solved in nearly the same form but with a predictor–corrector methodology. It can be seen that our novel treatment of viscoelasticity is a degenerate case of rate-dependent elastoplasticity with a collapsed elastic region for which (34)<sub>2</sub> is always satisfied. Different, more traditional techniques are shown in the book by Simo and Hughes [37].

At each iteration  $k$  of the Newton–Raphson method for solving the system (34), the linear system

$$\begin{bmatrix} \mathbb{M}_{pp} - \mathbb{I} & \underline{\mathbf{M}}_{py} \\ \underline{\mathbf{M}}_{Tp} & \underline{\mathbf{M}}_{Ty} \end{bmatrix}^k \begin{Bmatrix} \Delta\underline{\mathbf{C}}_v \\ \Delta(\Delta\gamma) \end{Bmatrix} = \begin{Bmatrix} \text{eq}_1 \\ \text{eq}_2 \end{Bmatrix}^k \quad (36)$$

is solved, and then the viscous right Cauchy–Green tensor and the viscous multiplier are updated as  $\underline{\mathbf{C}}_v^{k+1} = \underline{\mathbf{C}}_v^k + \Delta\underline{\mathbf{C}}_v$  and  $\Delta\gamma^{k+1} = \Delta\gamma^k + \Delta(\Delta\gamma)$ , respectively. Note that the subscripts  $n$  and  $n+1$  have been dropped for clarity. The linearized terms on the left-hand side of (36) are given by

$$\begin{aligned} \mathbb{M}_{pp} &= \mathbb{M}_{pT} \mathbb{M}_{Tp}, & \underline{\mathbf{M}}_{py} &= \mathbb{M}_z \underline{\mathbf{N}}, \\ \underline{\mathbf{M}}_{Tp} &= 2 \left( \frac{\partial T}{\partial \underline{\mathbf{C}}_v} T - \mathbb{M}_{Tp} \underline{\mathbf{T}} \right), & \underline{\mathbf{M}}_{Ty} &= 2T \frac{\partial T}{\partial \Delta\gamma}, \end{aligned} \quad (37)$$

where

$$\begin{aligned} \mathbb{M}_{pT} &= \Delta\gamma \mathbb{M}_z \frac{d\underline{\mathbf{N}}}{d\underline{\mathbf{T}}}, & \mathbb{M}_{Tp} &= -\mathbb{M}_e \mathbb{B}(\mathbf{F}) \mathbb{A}(\underline{\mathbf{C}}_v^{-1}), & \mathbb{M}_z &= 2\mathbb{A}(\mathbf{F}_v) \mathbb{N}_z, \\ \mathbb{M}_e &= \frac{d\underline{\mathbf{T}}}{d\underline{\mathbf{B}}_e}, & \mathbb{N}_z &= \frac{d\widehat{\text{exp}}(\mathbf{Z})}{d\underline{\mathbf{Z}}} \end{aligned} \quad (38)$$

and  $\mathbb{I}$  represents the fourth-order identity tensor. Fewer than 10 iterations are usually required to reach the tolerance  $\|\Delta\underline{\mathbf{C}}_v\|_{\mathcal{F}} \leq \text{tol} = 1 \times 10^{-8}$ . The accuracy of this solution affects the exactness of the tangent modulus.

Once the solution of (36) is obtained, the increment in the viscous multiplier is related to the increment in the viscous right Cauchy–Green tensor by

$$\Delta(\Delta\gamma) = \underbrace{-\underline{\mathbf{M}}_{Ty}^{-1} \underline{\mathbf{M}}_{Tp}}_{\underline{\mathcal{M}}_{Tp}} \Delta\underline{\mathbf{C}}_v, \quad (39)$$

and the time-derivative of  $\underline{\mathbf{C}}_v$  (taken with respect to the imposed  $\mathbf{F}$ ) yields

$$\frac{d\underline{\mathbf{C}}_v}{dt} = \underbrace{\star \underline{\mathcal{M}}_{pp}^{-1} \underline{\mathcal{M}}_{pT} \underline{\mathcal{M}}_{TL}}_{\underline{\mathcal{M}}_{pL}} : \underline{\mathbf{L}}, \quad (40)$$

where

$$\star \underline{\mathcal{M}}_{pp} = \mathbb{I} - \underline{\mathcal{M}}_{pp} - \underline{\mathbf{M}}_{py} \otimes \underline{\mathbf{M}}_{yp}, \quad \underline{\mathcal{M}}_e = \frac{d\underline{\mathbf{T}}}{d\underline{\mathbf{B}}_e}, \quad (41a)$$

$$\underline{\mathcal{M}}_{TL} = 2 \underline{\mathcal{M}}_e \underline{\mathbf{B}}_e. \quad (41b)$$

Here,  $\otimes$  denotes the tensor product. Note that  $\underline{\mathcal{M}}_{TL}$  is not minor-symmetric in the last two indices, and that the tensor multiplication in (41b) is made in the last index of  $\underline{\mathcal{M}}_e$  and the first of  $\underline{\mathbf{B}}_e$ . Finally, the tangent modulus  $\underline{\mathcal{C}}_{TL}$  used in (11), which relates the time derivative of  $\underline{\mathbf{T}}$  with the velocity gradient  $\underline{\mathbf{L}}$ , is given by

$$\underline{\mathcal{C}}_{TL} = \underline{\mathcal{M}}_{TL} + \underline{\mathcal{M}}_{Tp} \star \underline{\mathcal{M}}_{pp}^{-1} \underline{\mathcal{M}}_{pT} \underline{\mathcal{M}}_{TL} \quad (42)$$

and satisfies

$$\dot{\underline{\mathbf{T}}} = \underline{\mathcal{C}}_{TL} : \underline{\mathbf{L}} = (2 \underline{\mathcal{M}}_e \underline{\mathbf{B}}_e) : \underline{\mathbf{L}}_e = \underline{\mathcal{M}}_{TL} : \underline{\mathbf{L}}_e, \quad (43)$$

where  $\underline{\mathbf{L}}_e$  is the elastic velocity gradient. The Oldroyd modulus, employed in typical finite element implementations (in particular by Simo and Govindjee [14]), which can make use of the Lie derivative, is given by

$$\underline{\mathcal{C}}_{ijkl}^{\mathcal{L}} = \underline{\mathcal{C}}_{ijkl}^{TL} - T_{jl} \delta_{ik} - T_{il} \delta_{jk}, \quad (44)$$

where the minor-symmetry of  $\underline{\mathcal{C}}_{ijkl}^{\mathcal{L}}$  is preserved by definition. For the hyperelastic isotropic case, we can use the strain energy density function  $\hat{w}(\mathbf{B})$  to calculate the tangent modulus

$$\underline{\mathcal{C}}_{ijrs}^{TL} = 4\rho_0 B_{ik} \frac{\partial^2 \hat{w}}{\partial B_{ij} \partial B_{rm}} B_{ms} + T_{ij} \delta_{rs} + T_{is} \delta_{jr}. \quad (45)$$

Here, we use indicial notation for convenience, e.g.,  $[\underline{\mathbf{B}}]_{ik} = B_{ik}$ ,  $[\underline{\mathcal{C}}_{TL}]_{ijrs} = \underline{\mathcal{C}}_{ijkl}^{TL}$ .

Since we approximate the exponential function of a matrix numerically by Padé series, its derivative is of less cumbersome calculation. Specifically, we need to calculate  $\mathbb{N}_z = d\widehat{\text{exp}}(\mathbf{Z})/d\underline{\mathbf{Z}}$ . For the general case this is done by symbolic software, but in the simplest case it becomes

$$\mathbb{N}_z = -\underline{\mathbf{D}}_q^{-1} \frac{d\underline{\mathbf{D}}_q}{d\underline{\mathbf{Z}}} [\widehat{\text{exp}}(\mathbf{Z}) + \mathbf{1}], \quad (46)$$

where

$$\frac{d\underline{\mathbf{D}}_r}{d\underline{\mathbf{Z}}} = \sum_{j=0}^r \frac{(2r-j)! r!}{(2r)! j! (r-j)!} (-1)^j \mathcal{P}. \quad (47)$$

The term  $\mathcal{P}$  in (47) is the derivative of a matrix power, for which a relatively simple formula can be obtained

$$\underline{\mathcal{P}}_{rq} = \frac{d\underline{\mathbf{Z}}^t}{d\underline{\mathbf{Z}}_{rq}} = \sum_{s=0}^{t-1} \underline{\mathbf{Z}}^s \mathbf{J}_{rq} \underline{\mathbf{Z}}^{t-s-1}, \quad (48)$$

with

$$J_{rq} = \begin{bmatrix} 0 & 0 & 0 & 0 & 0 \\ 0 & \ddots & \vdots & \ddots & 0 \\ 0 & \dots & \underbrace{1}_{rq} & \dots & 0 \\ 0 & \ddots & \vdots & \ddots & 0 \\ 0 & 0 & 0 & 0 & 0 \end{bmatrix}$$

The costly tasks in these calculations are  $O(216)$  inversions and multiplications. Thus, row-based operations are implemented to minimize memory jumps. Note that  $\text{tr}(\mathbf{C}_v) = \text{tr}(\mathbf{B}_v)$ , and conversely for the elastic tensors. Therefore, switching from the spatial to the material description is a direct task when anisotropic hyperelastic behavior is modeled.

### 3.3. Specialization for a nonlinear material

Since the emphasis of this paper is on the nonlinear viscoelastic modeling of filled elastomers such as solid propellants, we employ the Bergström–Boyce viscoelastic model [6,7], which is an extension of the elastic Arruda–Boyce constitutive law [4]. This model can be viewed as a standard solid with spring element and Maxwell’s chain (spring and dashpot) [31].

In this model, the constitutive response of an elastomer is divided into a purely elastic response (represented by chain A) and a viscous response with an elastic component (chain B). Fig. 2 shows the main features of the chain split. The stress is then the sum of the two resultants, namely  $\mathbf{T}^A + \mathbf{T}^B$ , and the deformation equivalence is used ( $\mathbf{F} = \mathbf{F}^A = \mathbf{F}^B$ ). The deviatoric Kirchhoff stress is obtained as a product of the hardening shear modulus  $\mu_h$  and the deviatoric left Cauchy–Green elastic tensor

$$\mathbf{T}^A = \mu_h^A(\mathbf{B}) \text{dev} \mathbf{B}, \quad \mathbf{T}^B = \mu_h^B(\mathbf{B}_e) \text{dev} \mathbf{B}_e. \tag{49}$$

Note that the deviatoric operator ( $\text{dev}$ ) produces a trace-free tensor, ( $\text{tr}(\text{dev}(\cdot)) = 0$ ). If a volumetric term is included, it will be filtered out by the projection term (13) in our element formulation [1]. The hardening moduli  $\mu_h^{A,B}$  are given by

$$\mu_h^{A,B} = \mu_0 \mu_1 \mu_2 c_t, \tag{50}$$

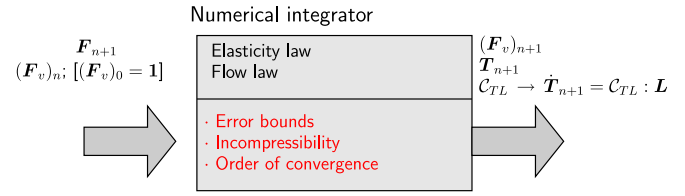


Fig. 3. Schematics of numerical integrator.

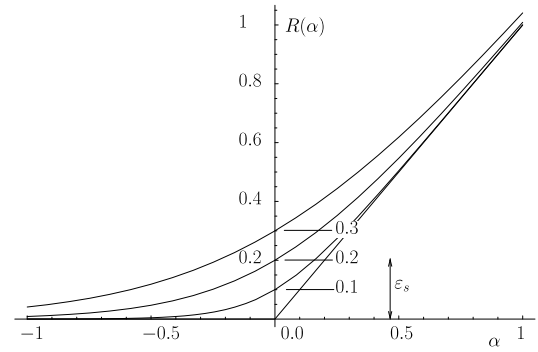


Fig. 4. Smooth ramp function.

where

$$\mu_0 = \frac{\mu}{\mathcal{L}^{-1}\left(\frac{1}{\lambda_l}\right)}, \quad \mu_1 = \frac{1}{\lambda_e}, \quad \mu_2 = \mathcal{L}^{-1}\left(\frac{\lambda_e}{\lambda_l}\right), \tag{51}$$

$$c_t = \det(\mathbf{B}_e)^{-\frac{1}{3}},$$

with  $\mu$  and  $\lambda_l$  being given material properties. The equivalent elastic stretch  $\lambda_e$  is calculated from the trace of  $\mathbf{B}_e$  and  $c_t$  as

$$3\lambda_e^2 = c_t \text{tr}(\mathbf{B}_e), \tag{52}$$

and the viscous equivalent stretch yields

$$\lambda_v = \sqrt{\frac{\text{tr}(\mathbf{C}_v)}{3}}, \quad \lambda_v \geq 1. \tag{53}$$

To compute the hardening modulus of the viscoelastic chain B, we use coefficients as given above. For chain A,  $\lambda_v = 1$  and we substi-

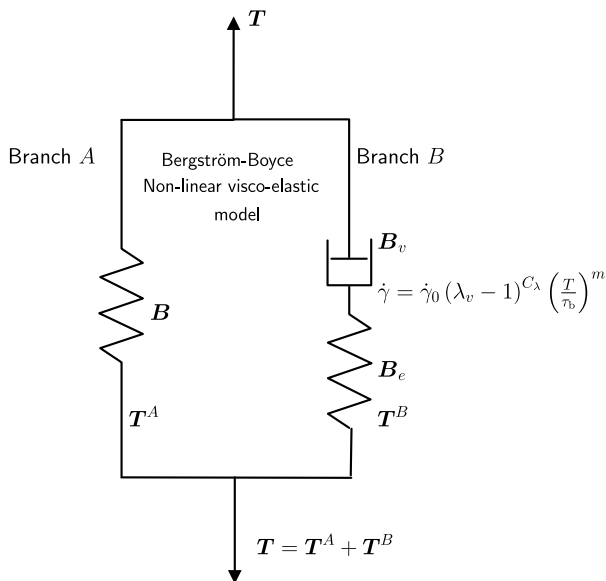


Fig. 2. Rheological representation of constitutive Bergström–Boyce model.

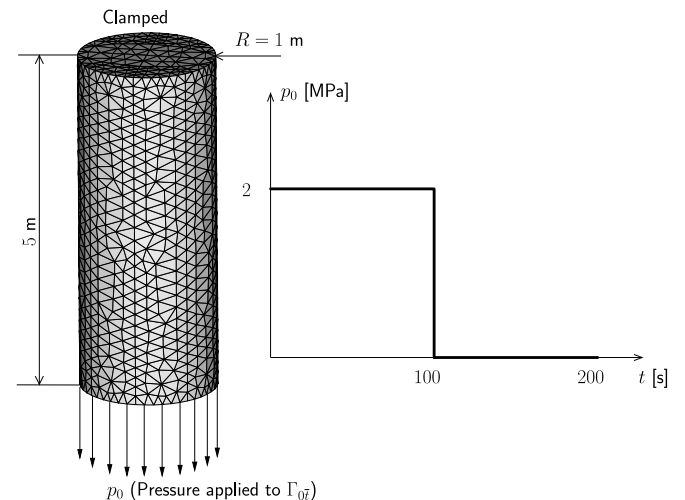


Fig. 5. Creep and relaxation test: geometry, boundary conditions, and loading history.

**Table 1**  
Properties of chloroprene rubber, taken from [6]

$\mu_A$	1.31 MPa
$\mu_B$	4.45 MPa
$\kappa_A = \kappa_B$	500 MPa
$\lambda_{IA} = \lambda_{IB}$	3
$\dot{\gamma}_0$	$0.33 \text{ s}^{-1}$
$C_\lambda$	-1
$m$	5.21
$\tau_b$	1 MPa

tute  $\lambda_e^A$  for  $\lambda_e$  and  $\mathbf{B}$  for  $\mathbf{B}_e$ , respectively. Note that in the case of elastic incompressibility,  $\lambda_e \geq 1$ . In (51), the function  $\mathcal{L}(\alpha)$ , called the Langevin function, is defined by

$$\mathcal{L}(\alpha) = \coth(\alpha) - \alpha^{-1}, \tag{54}$$

where both terms grow unbounded for  $\alpha \rightarrow 0$  but the function is still well defined at that point. To obtain the inverse (whose domain is  $] -1, 1[$ ), the Newton–Raphson iterative method is employed

$$\alpha(\beta) = \mathcal{L}^{-1}(\beta) = \text{arg}_\eta(\mathcal{L}(\eta) = \beta), \tag{55}$$

and the corresponding derivative is  $(\mathcal{L}^{-1})'(\beta) = 1/\mathcal{L}'(\alpha(\beta))$ . An alternative to this approach is to use the Lagrange–Bürmann formula [8]. To conclude the constitutive behavior, we define the equivalent flow strain rate as given by the Bergström–Boyce law

$$\dot{\gamma} = \dot{\gamma}_0 (\lambda_v - 1)^{C_\lambda} \left( \frac{T}{\tau_b} \right)^m, \tag{56}$$

with  $\dot{\gamma}_0, m > 0, C_\lambda \in [-1, 0]$ , and  $\tau_b$  being material properties. The inverse relation used in the integration algorithm (Section 3.1) reads

$$T = \tau_b (\lambda_v - 1)^{-\frac{C_\lambda}{m}} \left( \frac{\dot{\gamma}}{\dot{\gamma}_0} \right)^{\frac{1}{m}}. \tag{57}$$

We now investigate (56). It can be easily observed that for  $\lambda_v \leq 1$ , (56) would result in either a singularity or an inadmissible situation (since  $\dot{\gamma} \geq 0$ ). Although physically impossible (see (53)), such a situation can easily occur in the iterative scheme used to solve the system (36). A similar numerical problem is encountered when one wants to compute the elastic and viscous effective stretch tensors

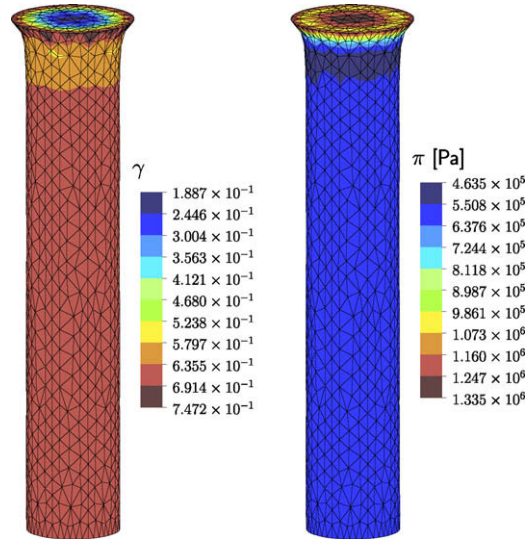


**Fig. 7.** Creep and relaxation test: contour plots of  $\gamma$  and pressure  $\pi$  for maximum stretch.

(52) and (53). Therefore, we replace certain nondifferentiable functions by differentiable ones using the smooth ramp formula

$$R(\alpha) = 2.8853 \varepsilon_s \left( 0.3466 + 0.1733 \frac{\alpha}{\varepsilon_s} - 0.5 \log \left\{ \frac{1}{\cosh \left[ 0.3446 \left( \frac{\alpha}{\varepsilon_s} \right) \right]} \right\} \right) \tag{58}$$

satisfying

$$\lim_{\alpha \rightarrow -\infty} \left( \frac{dR(\alpha)}{d\alpha} \right) = 0, \quad R(0) = \varepsilon_s, \quad \lim_{\alpha \rightarrow +\infty} \left( \frac{dR(\alpha)}{d\alpha} \right) = 1. \tag{59}$$

The function  $R(\alpha)$  is depicted in Fig. 4. For example, we replace  $\lambda_v - 1$  by  $R(\lambda_v - 1)$ , which is always positive. Similarly, we replace  $\lambda_e$  by  $R(\lambda_e)$  and  $\lambda_v$  by  $R(\lambda_v)$ . The proposed smoothing procedure was found to be beneficial for large time steps, and substantial drift from the actual solution was not observed for reasonable values of  $\varepsilon_s$ . In the examples presented hereafter, we use  $\varepsilon_s = 1 \times 10^{-3}$ .

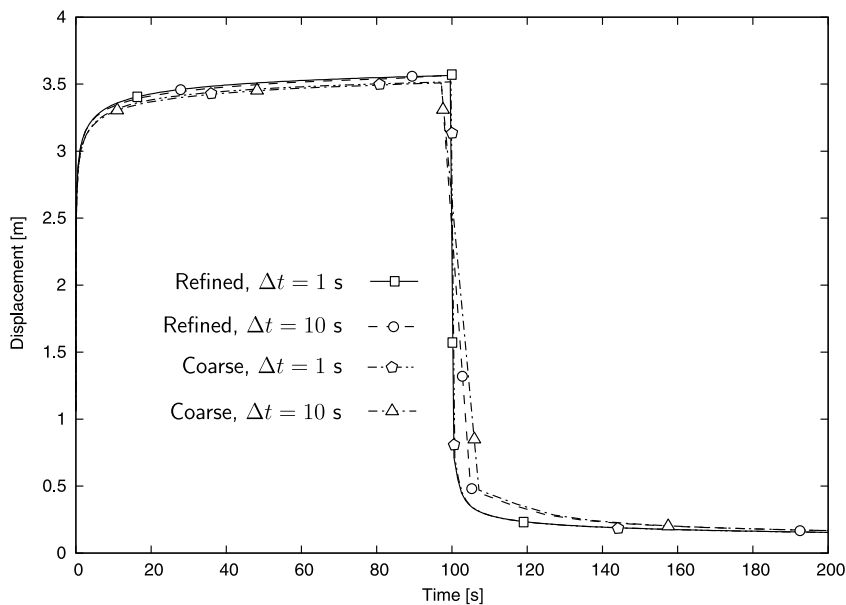


**Fig. 6.** Creep and relaxation test: creep and relaxation curves for various mesh discretizations and time steps.

To obtain the tangent modulus, we follow the formulation derived in Section 3.2 and apply it to either of the branches (A and B). We write

$$\dot{\mathbf{T}}^A = \mathcal{M}_{TL}^A : \mathbf{L}, \quad \dot{\mathbf{T}}^B = \mathcal{C}_{TL}^B : \mathbf{L}, \quad (60)$$

since by construction,  $\mathbf{L} = \mathbf{L}^A = \mathbf{L}^B$ . Here, the hyperelastic tangent modulus of chain A is obtained from (41b) and the viscoelastic tangent modulus of chain B is given by (42). To compute the tangent moduli (41b) and (42), one needs to evaluate several derivatives. For the elastic part, we have

$$\begin{aligned} \mathbb{M}_e = & -\frac{\det(\mathbf{B}_e)^{-4/3}}{3} \mu_0 \mu_1 \mu_2 \text{dev} \mathbf{B}_e \otimes \frac{d \det(\mathbf{B}_e)}{d \mathbf{B}_e} \\ & + \mu_0 \mu_1 (\mathcal{L}^{-1})' \frac{c_t}{2 \lambda_e \lambda_l} \frac{d \lambda_e^2}{d \mathbf{B}_e} \otimes \text{dev} \mathbf{B}_e - \mu_0 \mu_2 c_t \frac{1}{2 \lambda_e^3} \frac{d \lambda_e^2}{d \mathbf{B}_e} \otimes \text{dev} \mathbf{B}_e \\ & + \mu_0 \mu_1 \mu_2 c_t \left( \mathbb{I} - \frac{1}{3} \mathbf{1} \otimes \mathbf{1} \right), \end{aligned} \quad (61)$$

where the derivative of the determinant is given by

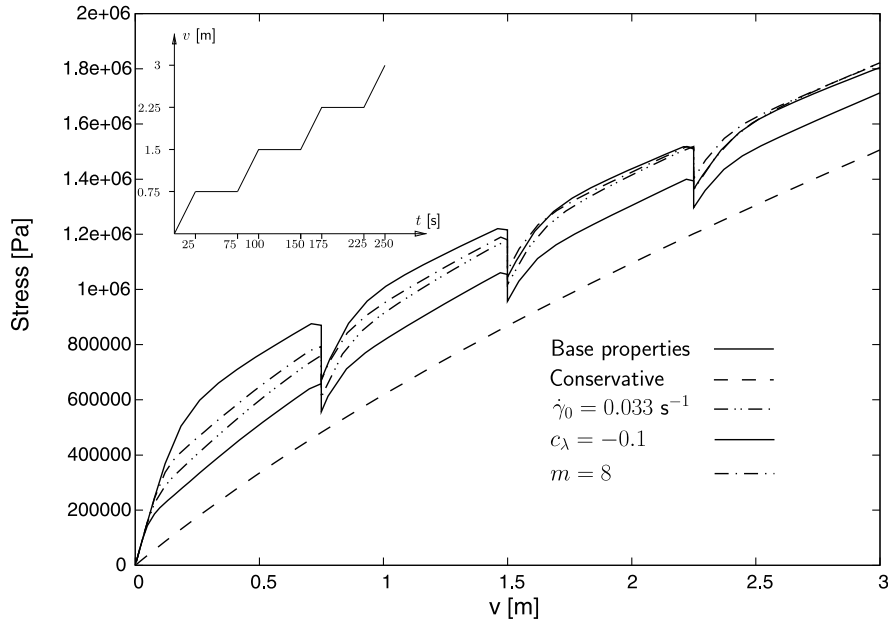


Fig. 8. Creep and relaxation test: effect of material properties.

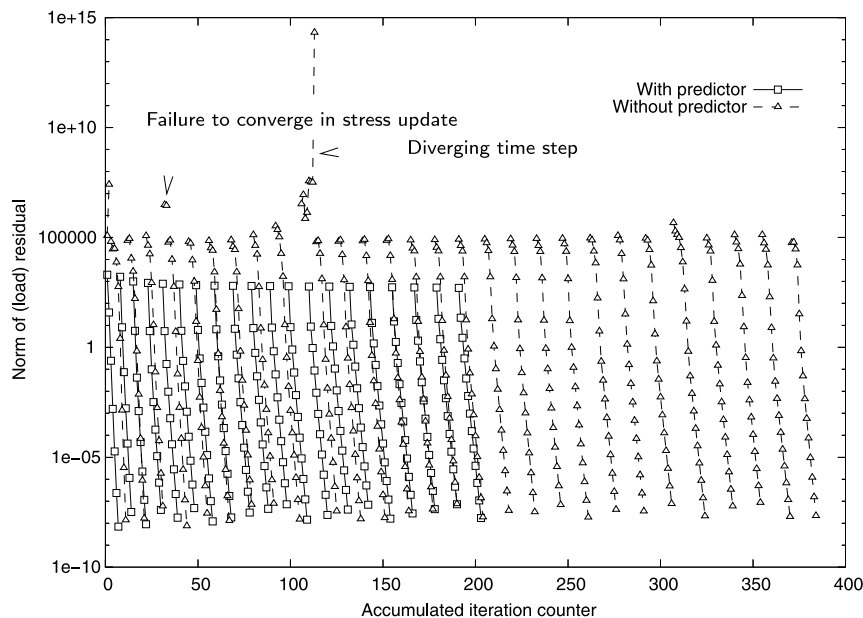


Fig. 9. Creep and relaxation test: convergence of load residual for case of proportional loading. Without predictor, 28 time steps are needed, whereas with predictor only 20 time steps are needed.

$$\frac{d \det(\mathbf{B}_e)}{d \underline{\mathbf{B}}_e} = \begin{Bmatrix} B_{22e}B_{33e} - B_{23e}^2 \\ B_{11e}B_{33e} - B_{13e}^2 \\ B_{11e}B_{22e} - B_{12e}^2 \\ 2(B_{13e}B_{23e} - B_{12e}B_{33e}) \\ 2(B_{12e}B_{23e} - B_{13e}B_{22e}) \\ 2(B_{13e}B_{12e} - B_{23e}B_{11e}) \end{Bmatrix}. \quad (62)$$

Note the coefficient 2 in the shear terms, which is required to obtain a correct product and follows from symmetry replacement invoked before calculating the derivative. We use the convention (11, 22, 33, 12, 13, 23) to order the components of symmetric tensors. The viscous components are then given by

$$\begin{aligned} \frac{\partial T}{\partial \underline{\mathbf{C}}_v} &= -\frac{\tau_b C_\lambda}{3m} \left(\frac{\dot{\gamma}}{\dot{\gamma}_0}\right)^{\frac{1}{m}} (\lambda_v - 1)^{-\frac{c_\lambda + m}{m}} \hat{\mathbf{1}}, \\ \frac{\partial T}{\partial \Delta \gamma} &= \frac{\tau_b}{\Delta t m \dot{\gamma}_0} \left(\frac{\dot{\gamma}}{\dot{\gamma}_0}\right)^{\frac{1+m}{m}} (\lambda_v - 1)^{-\frac{c_\lambda}{m}}, \end{aligned} \quad (63)$$

where  $\hat{\mathbf{1}} = \{1, 1, 1, 0, 0, 0\}^T$  and the geometric term yields

$$\frac{d \mathbf{N}}{d \underline{\mathbf{T}}} = \frac{1}{\|\underline{\mathbf{T}}\|_{\mathcal{F}}} [\mathbf{0} - \mathbf{N} \otimes \underline{\mathbf{N}}]. \quad (64)$$

#### 4. Numerical tests

To demonstrate the capabilities of the proposed integration algorithm using the finite element scheme, we solve several viscoelastic examples. The first part is focused on viscoelastic parameter influence, general model capability and a validation study. The last example is devoted to analysis of the unit cell for a solid propellant.

##### 4.1. Creep and relaxation test

The purpose of this test is to study the effect of mesh size and time step size, and to investigate the influence of material properties and the convergence of the nonlinear scheme. A typical version of the creep–relaxation test is employed for a clamped cylindrical specimen loaded in tension by a longitudinal force over the time interval from  $t_0 = 0$  s to  $t_f = 100$  s. The geometry, boundary conditions, and loading history are shown in Fig. 5. The specimen is

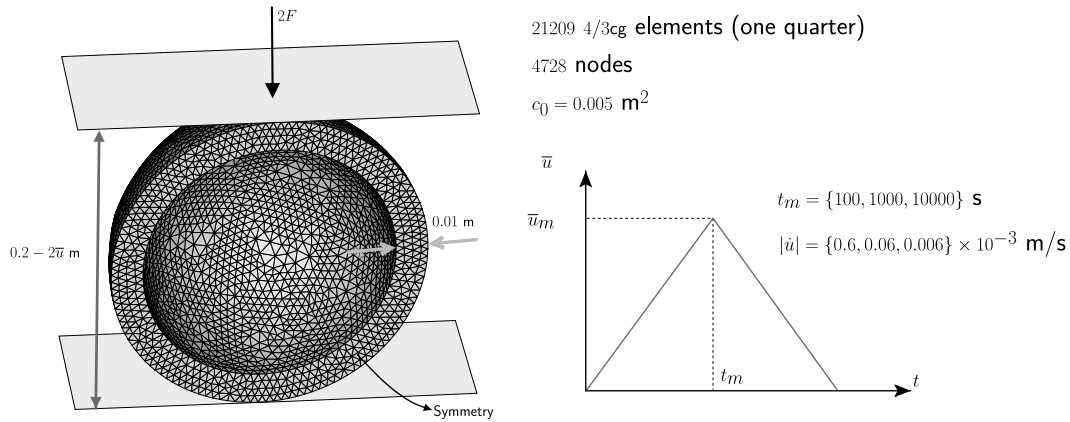


Fig. 10. Hollow sphere compression test: geometry, boundary conditions, and loading history.

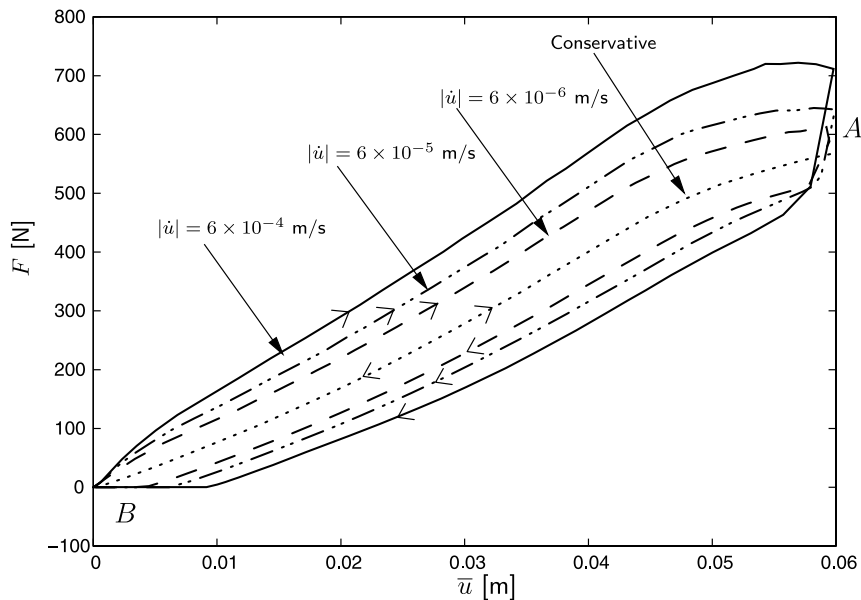


Fig. 11. Hollow sphere compression test: load versus displacement diagrams for three loading rates corresponding to  $t_m = \{100, 1000, 10,000\}$  s. Conservative case also shown.

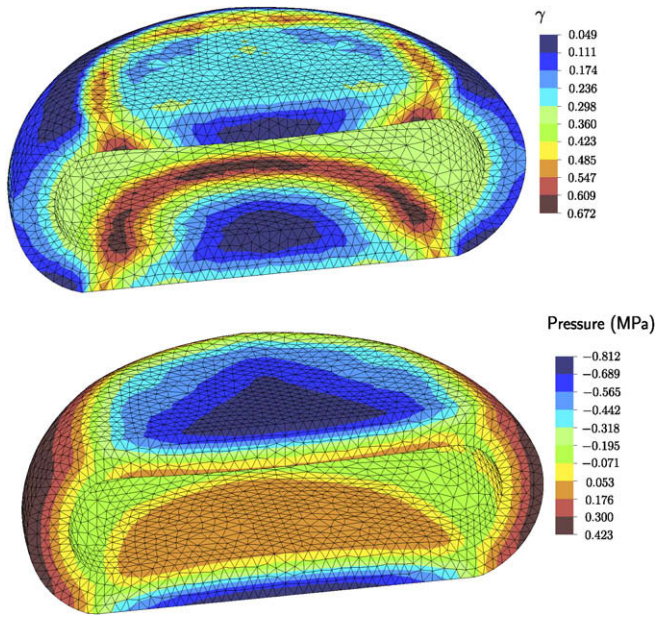


Fig. 12. Hollow sphere compression test: isocontours of accumulative effective shear parameter  $\gamma$  and pressure  $\pi$  for  $t = t_m = 100$  s.

made of a chlorprene rubber containing 15% carbon black N600 filler particles by volume (Table 1). Two different meshes were used, consisting of 1533 (coarse) and 4727 (fine)  $4/3c_g$  elements with  $c_0 = 3$  m<sup>2</sup>. Due to symmetry, only one quarter of the domain is modeled. We also investigated two different time steps,  $\Delta t = 10$  s and  $\Delta t = 1$  s. No adaptive time stepping is used for this problem. Fig. 6 shows the effect of both time step size and mesh refinement on the creep–relaxation curve. Good agreement is obtained between the results corresponding to the two meshes over the loading history, verifying the spatial convergence of the numerical solution. The time step size shows some sensitivity, especially after the unloading, but this influence decays for a longer relaxation period. To quantify the extent of viscous flow, we define the equivalent cumulative shear strain measure

$$\gamma = \int_0^t \dot{\gamma} dt. \tag{65}$$

Fig. 7 shows the cumulative shear  $\gamma$  and the pressure field for the loading time  $t = 100$  s (time before unloading); substantial material flow can be observed.

To understand further the influence of the individual parameters in the Bergström–Boyce nonlinear viscoelastic model on the numerical solution, we elongate the bar described above in a sequence of loading steps (uniaxial displacement is prescribed as shown in the insert to Fig. 8). The finer mesh and adaptive time stepping are used for this example. Each parameter of the Bergström–Boyce law is perturbed from its base value given in Table 1. Note that the  $\tau_b$  parameter (see (56)) is redundant and thus is not investigated hereafter. The corresponding sensitivities to material parameters, together with the response of the baseline and the hyperelastic (conservative) solutions, are shown in Fig. 8. Decreasing  $\dot{\gamma}_0$  stiffens the dashpot and results in increased stress, since the dashpot displacement is reduced. Increasing  $c_i$  has the effect of increasing the stress for the early stages of deformation, but its influence is attenuated when  $\lambda_v$  is no longer close to 1. Increasing the scaled stress exponent,  $m$ , produces more flow for  $\tau/\tau_b > 1$  and less flow otherwise.

The evolution of the load residual for proportional loading is shown in Fig. 9 (uniaxial displacement  $v = 3.5$  m is applied in several loading steps over  $\Delta t = 350$  s). We investigated two nonlinear solution strategies based on the Newton–Raphson method, one with and one without the force–displacement predictor, which is based on the linearized force corresponding to the imposed displacement increment. For both strategies we observed a quadratic rate of convergence. However, when attempted without the predictor, several diverging time steps were encountered. A convergence problem was encountered when the integration algorithm failed, and a second one was associated with failure to attain the radius of convergence. Moreover, the predictor decreased the number of time steps required to complete the analysis. Adaptive time stepping was used in both cases.

#### 4.2. Hollow sphere compression test

To investigate the effect of rate dependence on both loading and unloading response, we solved a hollow sphere problem. The

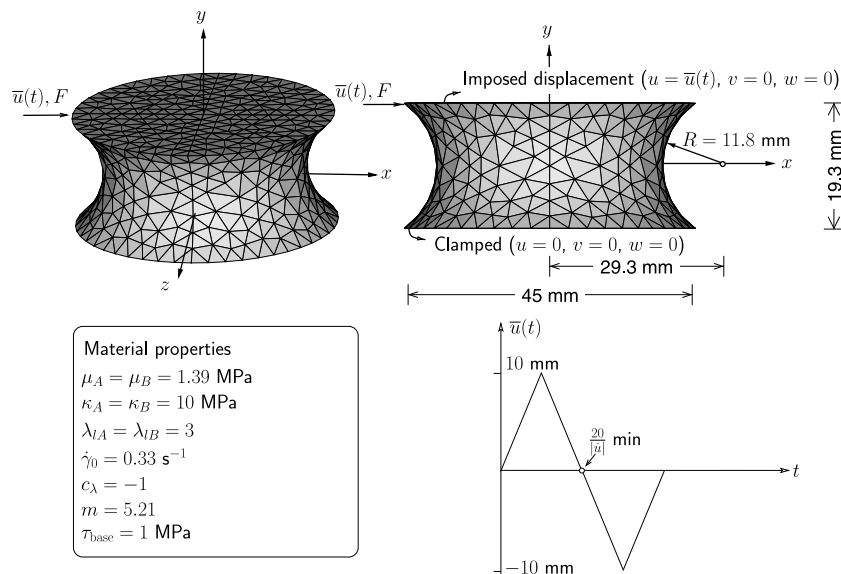
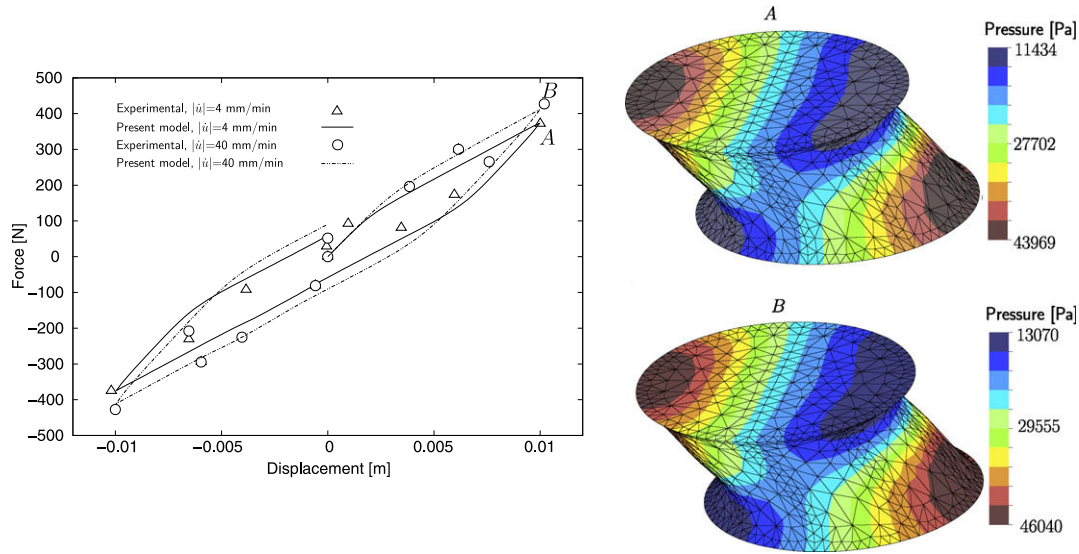


Fig. 13. Shear test validation: rubber specimen under cyclic loading. Dimensions, boundary conditions, loading, and material properties taken from paper by Miehe and Göktepe [27].



**Fig. 14.** Shear test validation: force–displacement curves (left) and distribution of pressure for both loading rates at points A and B (right). Experimental results, represented by symbols, are taken from [27].

**Table 2**  
Estimated mechanical properties of individual constituents

AP particles		Blend – small particles + binder	
$\mu$	132.34 GPa	$\mu_A$	2.9566 MPa
$\kappa$	213.35 GPa	$\kappa_A$	163 MPa
$\lambda_l$	3	$\mu_B$	2.9566 MPa
		$\kappa_B$	163 MPa
		$\lambda_{lA}$	3
		$\lambda_{lB}$	3
		$\dot{\gamma}_0$	0.33 s <sup>-1</sup>
		$C_s$	-1
		$m$	5.21
		$\tau_b$	1 Pa

relevant data for this test are shown in Fig. 10. The material properties correspond to chloroprene rubber and are the same as those used in the previous example. Two planes compress the sphere with a certain velocity, which is a function of time, and the loading/unloading response is monitored.

Fig. 11 shows marked growth in energy dissipation, with the rate dependent material stiffening as a function of the displacement  $\bar{u}$ , for different loading velocities. Note that the displacement

in the abscissa corresponds to plane motion, and when the loading process is reversed to unloading at time  $t_m$ , the loading plane moves away from the sphere, but the sphere in contact does not react instantaneously due to its viscoelastic nature. This leads to a sudden drop in the transmitted force (region A in Fig. 11), which is a function of the loading rate and the material relaxation time. Faster loading leads to a larger decline as the material does not have time to relax. A similar situation appears after the complete unloading (region B in Fig. 11). As one can see, the reaction is zero and a noticeable gap develops before the sphere regains its original shape. Note that the volume remains constant throughout the whole loading history.

The pressure and effective shear strain distributions are shown in Fig. 12. We observe that the distribution of  $\pi$  is smoother than the distribution of  $\gamma$  due to the smoothing introduced by (8).

### 4.3. Shear test validation

In order to validate our computational scheme, we compare it with results presented by Miehe and Göktepe [27], who introduced a micromechanics based microsphere model to represent viscoelasticity of elastomers. Relevant geometry, boundary and loading conditions, and material properties are shown in Fig. 13. The spec-

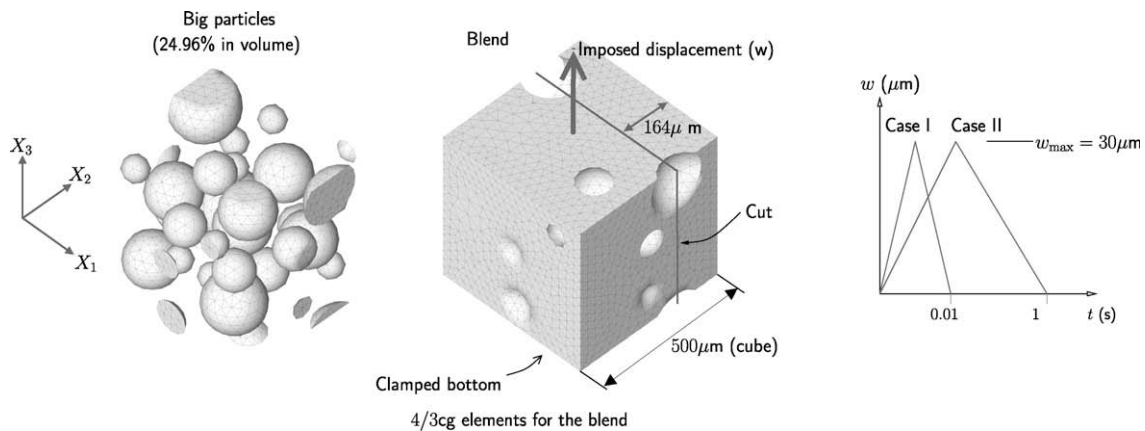


**Fig. 15.** Solid propellant unit cell: geometry, boundary conditions, and loading history.

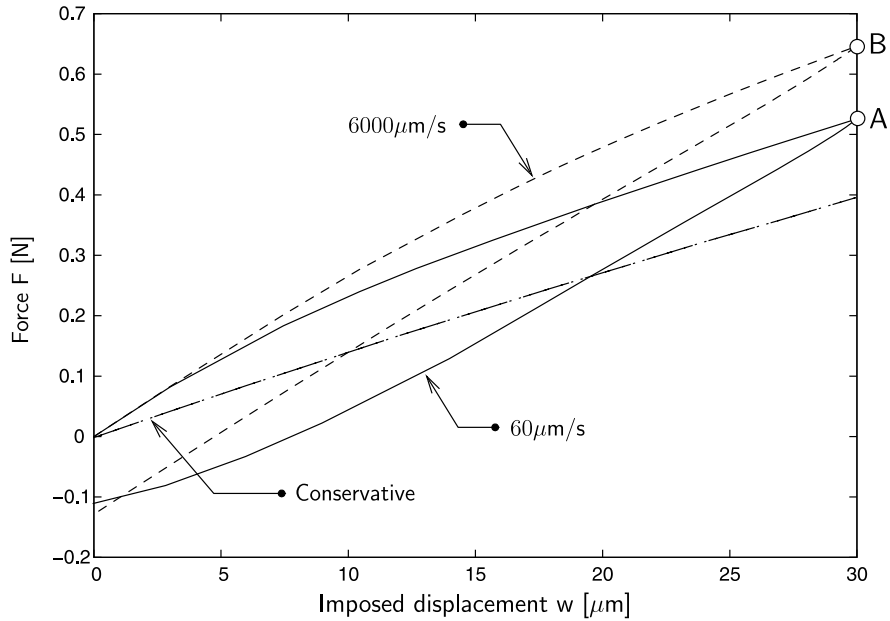


Fig. 16. Solid propellant unit cell: force–displacement curves for two loading rates as well as hyper-elastic case.

imen is made of a highly saturated nitrile HNBR50 rubber. The computational mesh consists of 3938  $4/3_{cg}$  elements with  $c_0 = 3 \text{ mm}^2$ . Note that Miehe and Göktepe employed a regular mesh containing 1152 mixed hexahedra elements with constant pressure, which is finer than ours, since each hexahedron can be divided into 4 tetrahedra. A cyclic horizontal displacement,  $\bar{u}(t)$ , is imposed with the two loading rates  $|\dot{\bar{u}}| = 40 \text{ mm/min}$  and  $|\dot{\bar{u}}| = 4 \text{ mm/min}$ .

Fig. 14 (left) displays the validation against the experimental data for both loading rates. Viscoelastic rate dependent stiffening is observed again. We see reasonable agreement between our model and the experimental results. Fig. 14 (right) shows the pressure field at the maximum loading points A and B, respectively. Pressure smoothness, weakly enforced by (10), is apparent once more.

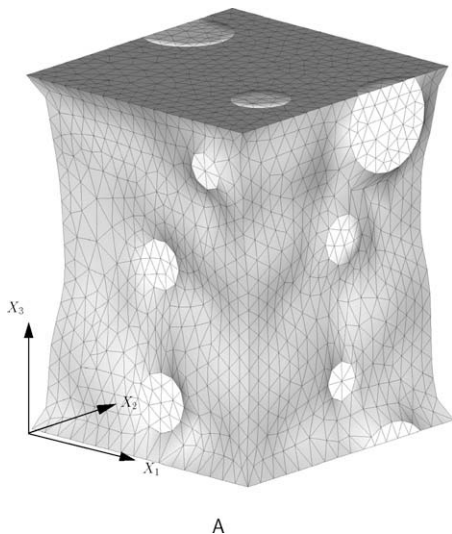


Fig. 17. Solid propellant unit cell: deformed shape showing flow of blend around stiff particles at loading point A in Fig. 16. Different shades of gray are caused by incident lighting and display inhomogeneous deformation of cell's surface.

#### 4.4. Solid propellant unit cell

To illustrate and test the proposed numerical framework for a complex heterogeneous material, we analyze a 27-particle composite system and demonstrate the ability of the numerical scheme to capture the effect of nonuniform particle spacing and size. To achieve high energetic content, solid propellants are typically characterized by high particle volume fractions (60–70%) obtained through a bimodal distribution of particle sizes. The mean diameter of small particles is about  $20 \mu\text{m}$ , while that of the larger particles is in the range  $100\text{--}300 \mu\text{m}$ . We focus on an idealized solid propellant composed of ammonium perchlorate (AP) particles (63%) embedded in a polymeric binder (37%). The particles are assumed to be hyperelastic, while the binder can undergo both elastic and viscous behavior and is represented by the Bergström–Boyce model. In the examples presented below, we assume a 63% concentration of AP particles, with 25% of large particles. The remaining 38% of small particles is then combined with the 37% of binder to create a homogenized matrix (blend). The elastic mechanical properties of the blend are obtained by homogenization [23]. Although some material data are known for solid propellants at the macroscopic level [29], the viscoelastic properties of individual constituents are not easily available. Thus, for the blend, we selected the same viscous properties as those for the reinforced rubber. The material constants are listed in Table 2. The geometry of the unit cell together with boundary conditions and two loading programs are shown in Fig. 15. It is important to note that in this example the strictly homogeneous boundary conditions are applied on the heterogeneous medium, which is cut out from the larger material sample. Such geometry and boundary conditions are selected here to imitate those applied to the material sample loaded inside the micro-CT (micro computed tomography) scanner. However, this choice of boundary conditions affects the extracted average constitutive properties, presented below in terms of force–displacement curves. The mesh contains 38793  $4/3_{cg}$  elements with  $c_0 = 3 \mu\text{m}^2$  discretizing the blend and 14101 traditional displacement-based elements discretizing particles (particles are compressible).

Fig. 16 shows the force–displacement curves for both loading rates as well as the response of the hyperelastic (conservative)

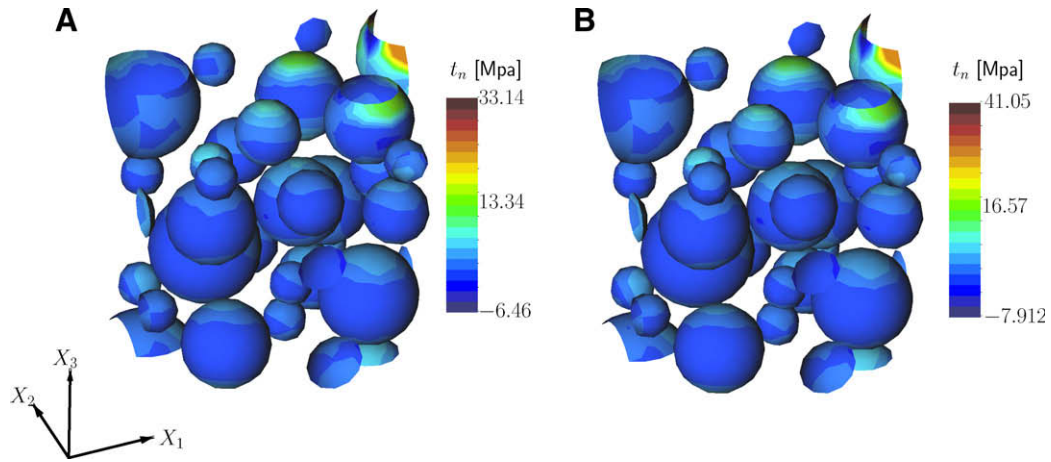


Fig. 18. Solid propellant unit cell: normal tractions along particle-matrix interface for loading points A and B in Fig. 16.

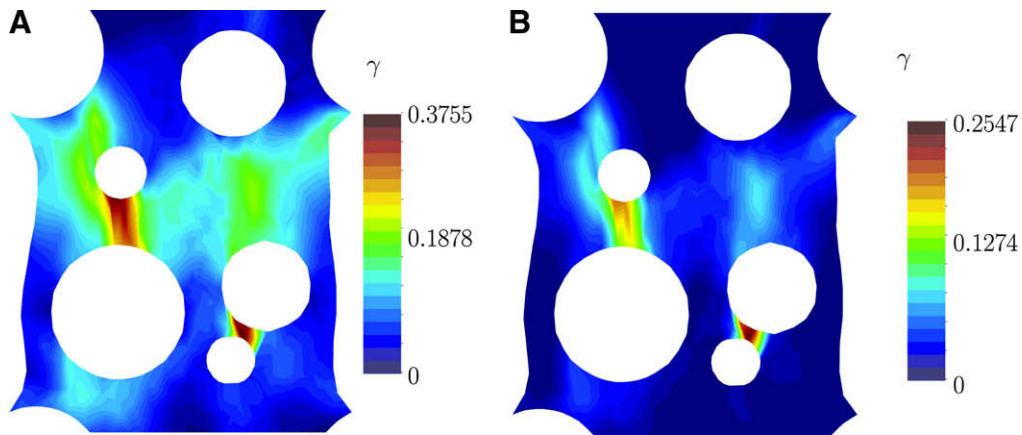


Fig. 19. Solid propellant unit cell: effective viscous strain,  $\gamma$ , in matrix for both loading paths (points A and B in Fig. 16). Cut-off plane shown in Fig. 15 is  $X = \{0, 336, 0\}$  and  $N = \{0, -1, 0\}$ .

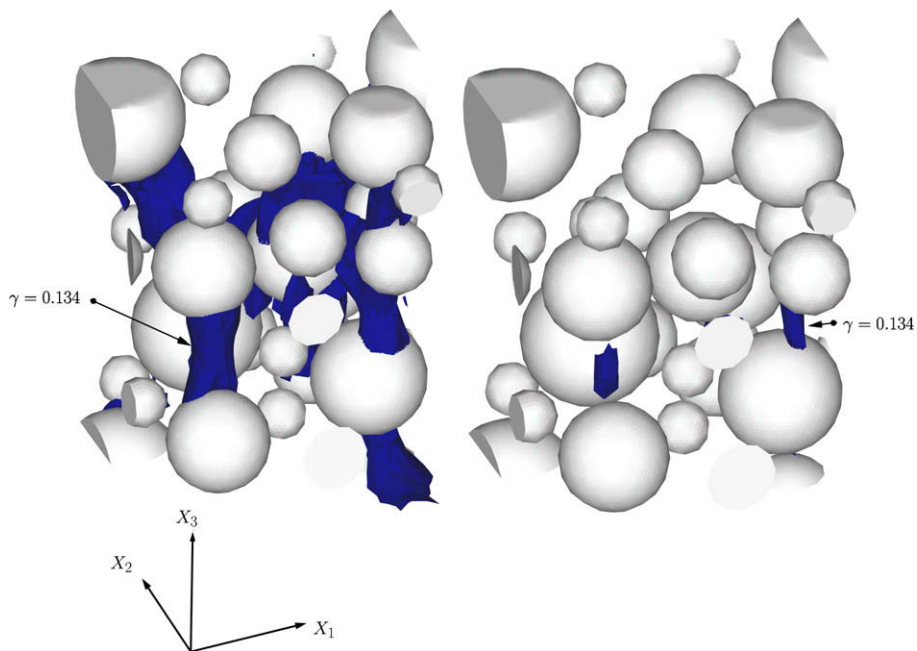


Fig. 20. Solid propellant unit cell: isocontours of accumulated viscous strain,  $\gamma$ , for slow (point A) and fast (point B) loading.

system. The rate sensitivity is apparent. Note the presence of a negative reaction at the end of the loading program, which is induced by forcing the unrelaxed viscoelastic material back to its original state. The deformed geometry for maximum elongation (point A) is depicted in Fig. 17, where we observe bulging of the blend around the stiff particles. Similar deformed geometry is obtained for the second loading path (point B) as well and is not displayed here. To assess potential particle debonding, we plot the normal tractions along the particle surface (Fig. 18). Stress concentrations are visible at the top and bottom poles of the particles, which is consistent with the loading direction. The highest concentration is then encountered in the regions of applied displacement, since the cut particles introduce highly favorable geometry.

To investigate the effect of particle-to-particle interactions on the viscous flow, we plot the isocontours of the effective cumulative shear parameter  $\gamma$  (see (65)) in Fig. 19. It is apparent that the highest material flow is in regions of high stress concentration due to the proximity of particles. We observe in Fig. 19 that for the slow loading rate (point A) the viscous field is more developed inside the matrix and that higher values of  $\gamma$  are obtained. The higher loading velocity stiffens the material, on the other hand, and thus the flow is concentrated predominately in regions of close particle proximity. To understand the spatial distribution of the viscous flow, we plot the isosurface of cumulative shear  $\gamma = 0.134$  at both loading points (points A and B in Fig. 16) in Fig. 20. As expected, the structure of  $\gamma$  is more developed for the slow loading rate, as the viscous regions connect particles in the principal strain direction. Surprisingly, only small material regions flow for the loading rate 6000  $\mu\text{m/s}$ , and larger strains would be required for fully developed viscosity.

### 5. Conclusions

We have formulated a novel integration algorithm and implemented it into a three-dimensional computational framework to simulate the viscoelastic response of reinforced elastomers. Both material and geometric nonlinearities are treated and the Bergström–Boyce viscoelastic model is employed. The finite element framework used in our work is based on a mixed Galerkin method with a nonlocal pressure field and a stabilization bubble, but a different numerical scheme can be used to solve the underlying PDE.

The highly nonlinear viscous constitutive law is integrated by a new second-order, unconditionally stable exponential integrator based on a diagonal Padé approximation. Exact preservation of a unit determinant of a traceless second-order tensor in 2D and the supremum and infimum of determinant in 3D are obtained. A consistent linearization of the resulting system of nonlinear equations has been derived and leads to an efficient solution of the complex, highly nonlinear problem.

Various viscoelastic examples were solved. Large magnitude stretches (75%) can be instantaneously applied with the proposed numerical scheme. To illustrate the ability of the numerical scheme to capture the effect of nonuniform particle spacing and size on viscous flow, we have analyzed a 27-particle composite system (an idealized solid propellant). The method was shown to capture the viscous flow due to stress concentrations in the vicinity of the particles.

The emphasis of this work has been on the development of a three-dimensional computational framework for the simulation of highly nonlinear viscoelastic reinforced elastomers. For many materials, such as solid propellants, it should also incorporate particle–matrix decohesion and matrix tearing. These two requirements will increase the computational costs associated with the analysis, therefore requiring an efficient parallel implementation of the computational scheme.

### Acknowledgements

The authors gratefully acknowledge support from Alliant Techsystems (ATK-21316), with J. Thompson and Dr. I.L. Davis serving as program monitors, and from the Center for Simulation of Advanced Rockets (CSAR) under Contract No. B523819 by the US Department of Energy as a part of its Advanced Simulation and Computing program (ASC). The authors also thank Prof. Michael Heath for numerous suggestions that improved the presentation of this paper.

### Appendix A

#### A.1. Error analysis and bounds of Padé approximation

Here, we present an error analysis of the integrator introduced in Section 3.1. As pointed out by Moler and Van Loan [28], the Padé approximation is more accurate near the origin. Taking advantage of this fact, we use the “scaling and squaring” method described in detail in [28], which corresponds to the approximation

$$\widetilde{\exp}_q^j(\mathbf{Z}) = \left[ \widetilde{\exp}_q \left( \frac{1}{2^j} \mathbf{Z} \right) \right]^{2^j}, \tag{A.1}$$

where  $\widetilde{\exp}_q^j(\mathbf{Z}) = \exp(\mathbf{Z} + \mathbf{E})$  with  $\mathbf{E}$  being the error matrix. There are two error controlling parameters,  $j$  and  $q$ , and it can be shown that the relative error has the upper bound

$$\frac{\|\mathbf{E}\|_{\mathcal{F}}}{\|\mathbf{Z}\|_{\mathcal{F}}} \leq 8 \left[ \frac{\|\mathbf{Z}\|_{\mathcal{F}}}{2^j} \right]^{2q} \left[ \frac{(q!)^2}{(2q)!(2q+1)!} \right] \tag{A.2}$$

for  $2\|\mathbf{Z}\|_{\mathcal{F}} \leq 2^j$ . If we use the smallest natural number  $j$  that satisfies  $2\|\mathbf{Z}\|_{\mathcal{F}} \leq 2^j$ ,  $j = j_{\text{opt}} \equiv \text{INT}[\log_2(2\|\mathbf{Z}\|_{\mathcal{F}})]$ , then we conclude that  $\varepsilon(j_{\text{opt}}, 1) \leq \frac{1}{6}$  and  $\varepsilon(j_{\text{opt}}, 2) \leq \frac{1}{2880}$ , etc. The Taylor series expansion, which we indicate by subscript  $T$ , of  $\exp(\mathbf{Z})$  provides a relative error bound sequence  $\varepsilon_T(j_{\text{opt}}, 1) \leq 2$ ,  $\varepsilon_T(j_{\text{opt}}, 2) \leq 0.67$ , etc.

These bounds are calculated using the expansion of the logarithm function presented in [28]. Note that a two-term Taylor series ( $q = 1$ ) is often adopted in the backward Euler update, and that it has a larger upper bound than that of the diagonal Padé approximation.

#### A.2. Enforcement of incompressibility by Padé approximation

For incompressible constitutive laws, accumulation of integration drift can cause significant violation of the incompressibility constraint. Here, we investigate determinant preservation using the exponential function, since it maps the exponential of a matrix trace to the determinant of the same matrix exponential,  $\exp(\text{tr}(\mathbf{Z})) = \det(\exp(\mathbf{Z}))$ , and thus for a traceless  $\mathbf{Z}$  a unit determinant is obtained. This important property should also be approximately satisfied by the diagonal Padé approximation.

If a spectral decomposition of  $\mathbf{Z}$  is performed ( $\mathbf{Z}$  is symmetric,  $\mathbf{z}_\alpha \in \mathbb{R}$ )

$$\mathbf{Z} = \sum_{\alpha=1}^{n_{\text{sd}}} z_\alpha \mathbf{m}_\alpha \otimes \mathbf{m}_\alpha, \tag{A.3}$$

where  $\mathbf{m}_\alpha$  are the principal directions and  $z_{n_{\text{sd}}} = -\sum_{i=1}^{n_{\text{sd}}-1} z_i$ , then

$$\widetilde{\exp}_q(\mathbf{Z}) = \sum_{\alpha=1}^{n_{\text{sd}}} \left\{ \underbrace{\left[ 1 + \frac{2b_\alpha(q)}{1 - b_\alpha(q) + c_\alpha(q)} \right]}_{\widetilde{\exp}_q(z_\alpha)} \mathbf{m}_\alpha \otimes \mathbf{m}_\alpha \right\}, \tag{A.4}$$

with

$$b_x(q) = \sum_{j=1}^{(1+q)/2} \frac{q!(1-2j+2q)!}{(2j-1)!(2q)!(1-2j+q)!} z_x^{2j-1}, \quad (\text{A.5})$$

$$c_x(q) = \sum_{j=1}^{q/2} \frac{(2q-2j)!q!}{(2q)!(2j)!(q-2j)!} z_x^{2j}.$$

We now show that the *exactness* is obtained for the present case for  $n_{sd} = 2$  and show the upper and lower errors for  $n_{sd} = 3$ . If  $n_{sd} = 2$  all deviatoric symmetric matrices have the form:

$$\mathbf{a} = \begin{bmatrix} a_{11} & a_{12} \\ a_{12} & -a_{11} \end{bmatrix}, \quad (\text{A.6})$$

which results in the following property

$$\det \left[ \sum_{i=1}^n c_i \mathbf{a}^i \right] = \sum_{i=1}^n c_i^2 \det[\mathbf{a}^i]. \quad (\text{A.7})$$

Thus, the unit determinant is preserved by the Padé approximation. If  $n_{sd} = 3$ , we restrict ourselves to  $\|\mathbf{z}\|_{\mathcal{F}} = 1$  (unit  $\mathbf{z}$ :  $z_1^2 + z_1 z_2 + z_2^2 = 1/2$ ), which results in the values shown in Table A.1, obtained by the direct constrained minimization and maximization of the principal directions presented above.

### A.3. Second-order convergence of exponential integrator

The order of convergence of an integrator is measured by the number of terms in the Taylor series expansion that are reproduced from the original ODE (see, e.g., [19,36]). We begin by investigating the exponential function and the first-order Padé approximation (Hughes–Winget formula [18]). Results for other cases can be generated using the same mechanism. In this section, we discard the continuum mechanics notation and use  $\mathbf{x}$  for the (generic) unknown. The generic ODE is

$$\dot{\mathbf{x}} = \mathbf{A}(\mathbf{x})\mathbf{x}, \quad (\text{A.8})$$

where  $\mathbf{x}_0 = \mathbf{x}_{t=0}$ . If  $\Delta t$  is the time increment, then an integrator that passes the second-order convergence test should reproduce both first (F) and second (S) order tests

$$\begin{aligned} \mathbf{x}_i^F &= \mathbf{x}_{i0} + \Delta t A_{ij} \mathbf{x}_j, \\ \mathbf{x}_i^S &= \mathbf{x}_{i0} + \Delta t A_{ij} \mathbf{x}_j + \frac{\Delta t^2}{2} \left( A_{ij} A_{jk} \mathbf{x}_k + \frac{dA_{ij}}{d\mathbf{x}_k} A_{kr} \mathbf{x}_r \mathbf{x}_j \right), \end{aligned} \quad (\text{A.9})$$

where  $A_{ij} \equiv A_{ij}(\mathbf{x})$  and summation is implied by repeated indices. Therefore, the exponential integrator  $\mathbf{x}_n = \exp(\Delta t \mathbf{A}(\mathbf{x}_n)) \mathbf{x}_0$  is first-order accurate, since

$$\mathbf{x}_n = \mathbf{x}_0 + \Delta t \left[ \mathbf{1} - \Delta t \mathbf{x}_n \frac{d\mathbf{A}}{d\mathbf{x}_n} \right]^{-1} \Big|_{\Delta t=0} \mathbf{A} \mathbf{x}_n + \text{h.o.t.}, \quad (\text{A.10})$$

and second-order accurate because

$$\left( \frac{d\Delta t \exp(\mathbf{A})}{d\Delta t} \mathbf{x}_0 \right)_i = A_{ij} A_{jk} \mathbf{x}_{nk} + \frac{dA_{ij}}{d\mathbf{x}_k} A_{kr} \mathbf{x}_{nr} \mathbf{x}_{nj}, \quad (\text{A.11})$$

which is the expected result.

For the two-term diagonal Padé approximation, a near-trapezoidal form is obtained (the strict trapezoidal form is also second-order accurate)

$$\mathbf{x}_n = \mathbf{x}_0 + \frac{\Delta t}{2} \mathbf{A}(\mathbf{x}_0 + \mathbf{x}_n), \quad (\text{A.12})$$

which is first-order accurate since  $\lim_{\Delta t \rightarrow 0} \mathbf{x}_0 + \mathbf{x}_n = 2\mathbf{x}_n$ . After replacing this result in the calculation of the second derivative, we obtain

$$\frac{d^2 \mathbf{x}_i}{d\Delta t^2} = A_{ij} A_{jk} \mathbf{x}_{nk} + \frac{dA_{ij}}{d\mathbf{x}_k} A_{kr} \mathbf{x}_{nr} \mathbf{x}_{nj}, \quad (\text{A.13})$$

which is the exact second derivative. Analysis of the Padé integrator with more terms follows this same pattern.

## References

- [1] P. Areias, K. Matouš. Stabilized four-node tetrahedron with nonlocal pressure for modeling hyperelastic materials. *Int. J. Numer. Methods Engrg.*, in press, doi:10.1002/nme.2361.
- [2] P.M.A. Areias, T. Belytschko, Analysis of finite strain anisotropic elastoplastic fracture in thin plates and shells, *ASCE J. Aerospace Engrg.* 19 (4) (2006) 259–270.
- [3] D.N. Arnold, F. Brezzi, M. Fortin, A stable finite element for the stokes equation, *Calcolo* 21 (1984) 337–344.
- [4] E.M. Arruda, M.C. Boyce, A three-dimensional constitutive model for the large stretch behavior of rubber elastic materials, *J. Mech. Phys. Solids* 41 (2) (1993) 389–412.
- [5] E. Artioli, F. Auricchio, L. Beirão da Veiga, A novel 'optimal' exponential-based integration algorithm for von-mises plasticity with linear hardening: theoretical analysis on yield consistency, accuracy, convergence and numerical investigations, *Int. J. Numer. Methods Engrg.* 67 (2006) 449–498.
- [6] J.S. Bergström, M.C. Boyce, Constitutive modeling of the large strain time-independent behavior of elastomers, *J. Mech. Phys. Solids* 46 (5) (1998) 931–954.
- [7] J.S. Bergström, M.C. Boyce, Constitutive modelling of the time-dependent and cyclic loading of the elastomers and application to soft biological tissues, *Mech. Mater.* 33 (2001) 523–530.
- [8] M. Böl, S. Reese, Finite element modelling of rubber-like materials—a comparison between simulation and experiment, *J. Mater. Sci.* 40 (2005) 5933–5939.
- [9] P. Chadwick, *Continuum Mechanics*, second ed., Concise Theory and Problems, Dover Publications, 1999.
- [10] M. Chiumenti, Q. Valverde, C.A. de Saracibar, M. Cervera, A stabilized formulation for incompressible plasticity using linear triangles and tetrahedra, *Int. J. Plasticity* 20 (2004) 1487–1504.
- [11] A.I. Dorfmann, R. Ogden, A constitutive model for the Mullins effect with permanent set in a particle-reinforced rubber, *Int. J. Solids Struct.* 41 (2004) 1855–1878.
- [12] A.D. Drozdov, A.I. Dorfmann, Stress-strain relations in finite viscoelastoplasticity of rigid-rod networks: applications to the Mullins effect, *Continuum Mech. Thermodyn.* 13 (2001) 83–205.
- [13] E. Fancello, J.-P. Ponthot, L. Stainier, A variational formulation of constitutive models and updates in non-linear finite viscoelasticity, *Int. J. Numer. Methods Engrg.* 65 (2006) 1831–1864.
- [14] S. Govindjee, J.C. Simo, Mullins' effect and the strain amplitude dependence of the storage modulus, *Int. J. Solids Struct.* 29 (1992) 1737–1751.
- [15] P. Haurat, E. Kuhl, M. Ortiz, Diamond elements: a finite element/discrete-mechanics approximation scheme with guaranteed optimal convergence in incompressible elasticity, *Int. J. Numer. Methods Engrg.* 72 (2007) 253–294.
- [16] G.A. Holzapfel, *Nonlinear Solid Mechanics: A Continuum Approach for Engineers*, John Wiley & Sons, 2000.
- [17] T.J.R. Hughes, L.P. Franca, M. Balestra, A new finite element formulation for computational fluid dynamics: V. circumventing the Babuska–Brezzi condition: a stable Petrov–Galerkin formulation of the Stokes problem accommodating equal-order interpolations, *Comput. Methods Appl. Mech. Engrg.* 59 (1986) 85–99.
- [18] T.J.R. Hughes, J. Winget, Finite rotation effects in numerical integration of rate constitutive equations arising in large-deformation analysis, *Int. J. Numer. Methods Engrg.* 15 (12) (1980) 1862–1867.
- [19] J.D. Lambert, *Computational Methods in Ordinary Differential Equations*, Wiley, 1973.
- [20] D. Lasry, T. Belytschko, Localization limiters in transient problems, *Int. J. Solids Struct.* 24 (1988) 581–597.
- [21] E.H. Lee, Elasto-plastic deformation at finite strains, *ASME J. Appl. Mech.* 36 (1969) 1–6.
- [22] A. Lion, A physically based method to represent the thermo-mechanical behaviour of elastomers, *Acta Mech.* 123 (1997) 1–25.
- [23] K. Matouš, Damage evolution in particulate composite materials, *Int. J. Solids Struct.* 40 (6) (2003) 1489–1503.
- [24] K. Matouš, P.H. Geubelle, Finite element formulation for modeling particle debonding in reinforced elastomers subjected to finite deformations, *Comput. Methods Appl. Mech. Engrg.* 196 (2006) 620–633.
- [25] K. Matouš, P.H. Geubelle, Multiscale modeling of particle debonding in reinforced elastomers subjected to finite deformations, *Int. J. Numer. Methods Engrg.* 65 (2006) 190–223.

**Table A.1**

Lower and upper determinants of  $\widetilde{\exp}_q$  for  $\|\mathbf{z}\|_{\mathcal{F}} = 1$

$q$	Min	Max
1	0.96186	1.03965
2	0.86979	1
3	0.99340	1.00665
4	0.99918	0.99960
5	1.00002	1.00003
6	0.99999	0.99999

- [26] K. Matouš, H.M. Inglis, X. Gu, D. Rypl, T.L. Jackson, P.H. Geubelle, Multiscale modeling of solid propellants: from particle packing to failure, *Compos. Sci. Technol.* 67 (2007) 1694–1708.
- [27] C. Miehe, S. Göktepe, A micro-macro approach to rubber-like materials. Part II: the micro-sphere model of finite rubber viscoelasticity, *J. Mech. Phys. Solids* 53 (2005) 2231–2258.
- [28] C. Moler, C. Van Loan, Nineteen dubious ways to compute the exponential of a matrix, twenty-five years later, *SIAM Rev.* 45 (1) (2003) 1–46.
- [29] S. Ozüpek, E.B. Becker, Constitutive modeling of high-elongation solid propellants, *J. Engrg. Mater. Technol.* 114 (1992) 111–115.
- [30] R.H.J. Peerlings, R. de Borst, W.A.M. Brekelmans, J.H.P. de Vree, Gradient enhanced damage for quasi-brittle materials, *Int. J. Numer. Methods Engrg.* 39 (1996) 3391–3403.
- [31] A.C. Pipkin, *Lectures on Viscoelasticity Theory*, second ed., Springer-Verlag, 1986.
- [32] M.A. Puso, J. Solberg, A stabilized nodeally integrated tetrahedral, *Int. J. Numer. Methods Engrg.* 67 (2006) 841–867.
- [33] B. Ramesh, A.M. Maniatty, Stabilized finite element formulation for elastic-plastic finite deformations, *Comput. Methods Appl. Mech. Engrg.* 194 (2005) 775–800.
- [34] S. Reese, S. Govindjee, A theory of finite viscoelasticity and numerical aspects, *Int. J. Solids Struct.* 35 (1998) 3455–3482.
- [35] J.C. Simo, On a fully three-dimensional finite-strain viscoelastic damage model: formulation and computational aspects, *Comput. Methods Appl. Mech. Engrg.* 60 (1987) 153–173.
- [36] J.C. Simo, S. Govindjee, Non-linear B-stability and symmetry preserving return mapping algorithms for plasticity and viscoplasticity, *Int. J. Numer. Methods Engrg.* 31 (1991) 151–176.
- [37] J.C. Simo, T.J.R. Hughes, *Computational Inelasticity*, corrected second printing edition., Springer, 2000.
- [38] R. Tian, H. Matsubara, G. Yagawa, Advanced 4-node tetrahedrons, *Int. J. Numer. Methods Engrg.* 68 (2006) 1209–1231.
- [39] O.C. Zienkiewicz, J. Wu, Incompressibility without tears – how to avoid restrictions of mixed formulation, *Int. J. Numer. Methods Engrg.* 32 (1991) 1189–1203.